Bio-Design and Manufacturing (2026) 9:465–500
https://doi.org/10.1631/bdm.2500260

REVIEW

Tomographic volumetric bioprinting: from bioink design to resolution enhancement

Qilin Wu[1,3] · Chaofan He[1,3] · Tianhong Qiao[1,3] · Yuewei Chen[4] · Hongyao Shen[1,3] · Yong He[1,2,3]

Received: 21 May 2025 / Accepted: 22 August 2025

Abstract

Tomographic volumetric bioprinting (TVBP) is an emerging transformative technology in bio-manufacturing, distinguished by two exceptional capabilities: ultrafast fabrication (centimeter-scale constructs within tens of seconds) and unique compatibility with ultra-soft bioinks ($<10^2$ Pa). Despite its potential, TVBP remains in its infancy because of significant hurdles. These include the need to adapt conventional photocurable bioinks to TVBP's unique photopolymerization requirements and achieve sufficient resolution to replicate intricate multicellular structures. Therefore, this review outlines strategies to address these challenges, delving into (1) the development of suitable bioinks, (2) printing resolution optimization, and (3) rapid construction of complex biological structures and functions. Furthermore, the fundamental principles and evolution of projection slicing algorithms are explored, and the latest advancements in TVBP applications are summarized. Finally, we explore the future trajectory of this promising bio-manufacturing technology.

✉ Yuewei Chen
ywchen3@gzu.edu.cn

✉ Hongyao Shen
shenhongyao@zju.edu.cn

✉ Yong He
yongqin@zju.edu.cn

[1] State Key Laboratory of Fluid Power and Mechatronic Systems & Liangzhu Laboratory, School of Mechanical Engineering, Zhejiang University, Hangzhou 310027, China

[2] The Second Affiliated Hospital, Zhejiang University School of Medicine, Hangzhou 310027, China

[3] Zhejiang Key Laboratory of Additive Manufacturing Technology and Equipment, School of Mechanical Engineering, Zhejiang University, Hangzhou 310027, China

[4] School of Mechanical Engineering, Guizhou University, Guiyang 550025, China

Graphical abstract

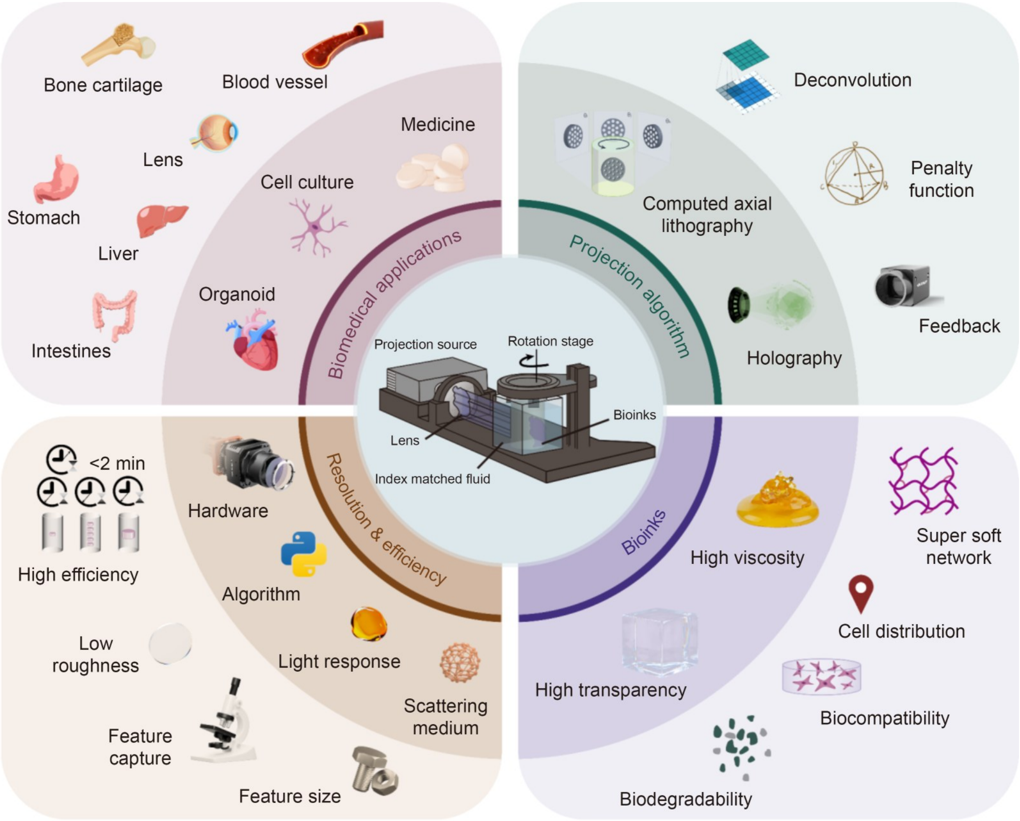

Keywords Volumetric printing · 3D printing · Bioprinting · Bioinks · Printing resolution

1 Introduction

Bioprinting is "the use of computer-aided transfer processes for the patterning and assembly of living and non-living materials with a defined 2D or 3D architecture to produce bioengineered structures" [1]. Several steps are required to implement bioprinting: (1) designing the overall print structure and bioprinting components (e.g., cells, bioinks, and biomaterial inks), (2) printing the desired construct with the appropriate bioprinter, and (3) processing the printed construct [2]. Precise layer-by-layer positioning of biomaterials, biochemical reagents, and living cells, along with spatial control over the placement of functional components, is implemented to fabricate 3D biostructures. Multiple methodologies fall under 3D bioprinting, including biomimicry, autonomous self-assembly, and mini-tissue building blocks. Compared with non-biological printing, 3D bioprinting entails additional complexities, such as the selection of materials, cell types, and growth and differentiation factors, with unique technical challenges related to the viability and sensitivity of living cells and tissue architecture [3]. 3D bioprinting has been used in the generation and transplantation of diverse tissues, including multilayered skin [4, 5], bone [6], vascular grafts [7, 8], tracheal-like structures [9], cardiac tissues [10], and cartilaginous structures [11]. High-throughput 3D bioprinting tissue models have also been developed for research, drug discovery, and toxicology [12].

The advancement of 3D printing technologies has significantly simplified the fabrication of objects with complex geometric structures. Photopolymerization-based curing technologies enable the rapid solidification of liquid resins through light-triggered polymerization or crosslinking reactions of photosensitive molecules. This process can be realized through sequential curing methods (e.g., stereolithography [13, 14] and digital light processing (DLP) [15–17]) and emerging volumetric curing techniques (such as multi-beam superposition printing [18], tomographic volumetric printing (TVP) [19–21], dual-wavelength synchronized curing (xolography) [22], and two-color light-sheet 3D micro-printing [23]). Furthermore, newer technologies such as filamented light (FLight) biofabrication [24, 25] and acoustic-based volumetric printing [26–28] are becoming widely known for their unique advantages. Voxel-based formation gives volumetric curing technologies a notable advantage in achieving printing speeds that far surpass conventional layer-by-layer methods [19, 29]. Continuous liquid interface production [30] and rapid DLP [31] offer comparable printing speeds in fabricating millimeter-scale models. Moreover, the entire printing process occurs within a deep vat, eliminating the need for support structures while enabling the direct fabrication of soft geometries with intricate cavities and overhanging features.

Among such technologies, TVP is currently the mainstream volumetric curing technology. In TVP, dynamic light patterns are projected from multiple angles to irradiate photopolymerizable liquid resins until the accumulated energy dose reaches the polymerization threshold, facilitating simultaneous solidification of the entire 3D object. Unlike most 3D printing approaches, TVP employs layerless fabrication. Instead of sequentially curing voxels, lines, or layers, it precisely constructs 3D geometries through continuous tomographic light pattern exposure. Typical printing durations range from tens of seconds for centimeter-scale objects, achieving resolutions as fine as 45–80 μm [20, 32]. High-power laser diodes further enhance printing efficiency. TVP also demonstrates exceptional material compatibility [33, 34] and has been successfully applied in fabricating various materials, such as acrylates [19, 35], thiol-ene photoresins [36–38], nanoparticle-loaded composites [20, 39–42], epoxy resins [43], and various cell-laden bioinks [21, 44–46]. Given its expanding biomedical applications, we propose the term “tomographic volumetric bioprinting (TVBP)” to distinguish it from the broader concept of volumetric bioprinting, which encompasses multiple volumetric curing technologies in biomanufacturing.

Recent reviews have systematically explored volumetric curing technologies while analyzing the commonalities and distinctions among different approaches [29, 47–50]. The current review examines TVBP, a rapidly developing volumetric curing technology with broad application prospects. We elaborate on its working principles, trace the evolution of slicing algorithms, and provide practical guidelines for bioink formulation based on empirical experience. Furthermore, we summarize the current methodologies for resolution assessment and thoroughly analyze factors influencing printing resolution, aiming to establish systematic manufacturing guidelines for achieving higher-resolution printing. Representative applications of TVBP are enumerated to demonstrate potential research directions. Finally, we summarize the existing challenges in TVBP applications and propose future development trajectories, hoping to collaborate with researchers worldwide to advance this promising technology.

2 Projection slicing algorithm

The core of TVP (alternatively named computed axial lithography (CAL) [19]) is in the voxel-selective solidification of photosensitive inks within enclosed volumes through photopolymerization. This fabrication approach is derived from computed tomography (CT) image reconstruction integrated with analogous dose-delivery methods, which is used in intensity-modulated radiation therapy (IMRT) [51, 52] for cancer treatment. In IMRT, precise 3D radiation exposure patterns are constructed to deliver therapeutic doses to tumor regions while minimizing exposure to surrounding organs. Similarly, in CAL, a coordinated 3D light dose distribution pattern is generated through multi-angle projections. This distribution precisely solidifies the ink into the desired geometries by exploiting the nonlinear response of photosensitive materials to optical doses, which occurs via the inhibition of oxygen [53] or other molecules [19, 20]. Figure 1 illustrates the fundamental principles and implementation workflow. The rendered model of Auguste Rodin’s sculpture, *The Thinker*, is used as an example (Fig. 1a). The algorithmic workflow for projection generation is grounded in the inverse problem of tomographic reconstruction. For a target geometry $f_T(\boldsymbol{r}, z)$, where $\boldsymbol{r}=(x, y)$ and $f_T=1$ denotes material presence (Fig. 1b), the optimal intensity projections $g_{\mathrm{opt}}(\boldsymbol{r}, \theta, z)$ must satisfy Eq. (1):

$$f(\boldsymbol{r}, z)=I\left\{\frac{\alpha}{\Omega}\left(T^*_{-\alpha}\left[g\right](\boldsymbol{r}, z)\right)\geq D_c\right\}, \tag{1}$$

where I is the indicator function implementing thresholding at the critical dose D_c, $T^*_{-\alpha}\left[g\right]$ is the exponential back-projection operator accounting for resin attenuation (coefficient α), and Ω is the container rotation rate.

The forward model is governed by the exponential Radon transform $T_\alpha\left[f_T\right]$ and its adjoint $T^*_\alpha\left[g\right]$ (Fig. 1c). To solve the inverse problem, filtered back-projection is used with attenuation compensation, as shown in Eq. (2):

$$g^{\pm}_{\mathrm{opt}}(\boldsymbol{r}, \theta, z)=\mathcal{F}^{-1}\left\{\hat{W}_\alpha(k)\cdot\mathcal{F}\left(T_\alpha\left[f_T\right]\right)\right\}, \tag{2}$$

where $\mathcal{F}$ and $\mathcal{F}^{-1}$ denote the Fourier transform (FT) and inverse FT, optimized via the fast FT algorithm, respectively, θ denotes the angle in the polar coordinate system, and f_T denotes the target geometry. The filter $\hat{W}_\alpha(k)=k\cdot I_{\{|k|>\alpha\}}$ acts as a high-pass ramp filter, suppressing frequencies below α and ensuring edge sharpness. In cases of negligible attenuation ($\alpha\approx0$), this filter reduces to the Ram–Lak filter.

2.1 Projection slice theorem connection

From the projection slice theorem in the $\alpha\approx0$ case, the 2D FT of the “flatland” target geometry for a given z slice is exactly equal to the one-dimensional (1D) FT of the integral projections along radial samples in the Fourier domain (Fig. 1d):

$$\hat{f}\left(\boldsymbol{k}, z\right) = \hat{T}_0\left[f\right]\left(\boldsymbol{k}\cdot\hat{\theta}, \theta, z\right), \tag{3}$$

where f denotes the printed geometry.

2.2 Iterative optimization

Since physical projectors require non-negative intensities, we formulate the reconstruction as a constrained optimization problem:

$$g_{\text{opt}} = \operatorname{argmin}\left\| f - f_{\text{T}} \right\|_2. \tag{4}$$

This is solved using projected gradient descent to minimize the L_2-norm discrepancy while enforcing $g \geq 0$. Furthermore, incorporating threshold nonlinearity into the problem is crucial for achieving a good correspondence between the dose curve and the target geometry.

The implementation workflow of TVP comprises four stages (Fig. 1e): (1) 3D model building, (2) projection image slicing, (3) projection printing, and (4) post-processing.

The algorithmic workflow for projection image slicing generally includes the following: (1) discretizing imported 3D models (STL format) into voxel grids, with each voxel labeled as 0 (non-cured region) or 1 (cured region), (2) applying exponential Radon transforms to each transverse slice (along the z-axis) to generate initial projection image sequences, (3) reconstructing 3D internal dose distributions through inverse exponential Radon transforms of current projections, (4) implementing iterative optimization cycles to minimize discrepancies between projected dose distributions and target models, (5) converting optimized projections into external projections aligned with actual projector coordinate systems, and (6) outputting final projection sequences.

In this subsection, we summarize the evolutionary trajectory of the slicing algorithm in TVP, and evaluate different optimization strategies and effects by analyzing several representative algorithm optimization examples (Fig. 2 and Table 1). In Sect. 4.2.4, we also discuss in detail the specific optimization strategies of some algorithms for print fidelity.

In 2019, Kelly et al. [19] proposed the projection gradient descent (PGD) method to address the 3D inverse problem underlying CAL. This heuristic finite-difference algorithm iteratively optimizes light intensity projections to

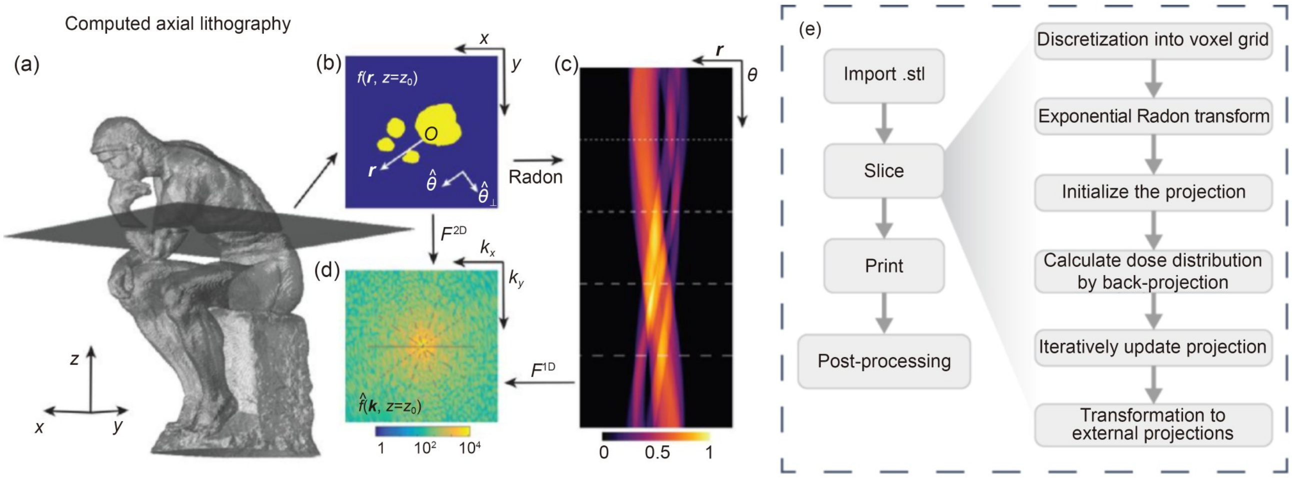

Fig. 1 Fundamental principles in tomographic volumetric printing (TVP): (a) 3D target object; (b) Z cross-section; (c) Radon transform; (d) 2D Fourier transform (FT); (e) implementation workflow of TVP. (a–d) are reproduced from [19], under exclusive license to AAAS

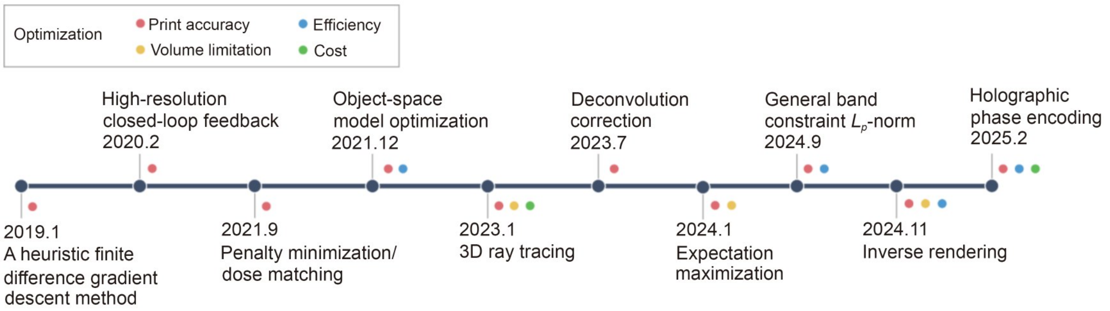

Fig. 2 Development of slicing algorithms in tomographic volumetric printing (TVP)

Table 1 Characteristics of different slicing algorithms

Algorithm	Targeted difficulties	Achieved resolution	Highlights
Heuristic finite difference gradient descent [19]	3D inverse problem underlying computed axial lithography (CAL)	300 μm	Pioneer work
High-resolution closed-loop feedback [32]	Accurate control of photopolymerization kinetics	80 μm (+) 500 μm (−)	High-resolution features
Penalty minimization (PM)/dose matching (DM) [54]	Quantitative description of the loss function	Deviations <1.05 mm	Meaningful metrics for quantitative comparison
Object-space model optimization (OSMO) [55]	Grayscale control for functionally graded materials	<200 μm	Improve the print accuracy of complex parts under imperfect material and optical precision
3D ray tracing [57]	Inherent 3D non-telecentricity in projector-based volumetric printing	200 μm	Three-fold increase in build volume without changes to hardware
Deconvolution correction [58]	Systematic under-curing of fine features	195 μm	A quantitative printing process prediction model
Expectation maximization (EM) [59]	High-attenuation ink (10 mm transmittance lower than 10%) or large-scale (diameter >100 mm)	<1 mm	Achieve high-fidelity printing for large volumes or using high-attenuation materials
General band constraint L_p-norm minimization [62]	Compatibility of the loss function	<200 μm	Generalization of previous optimization schemes
Inverse rendering [63]	Accurate control of the ray in scattering resins	<100 μm	Utilization of non-standard setups and surface-aware discretization that reduces resolution-related artifacts
Holographic phase encoding [64]	Amplitude coding with diffraction-limited resolution	31 μm	High light-projection efficiency

match the curing threshold of target geometries. However, the inherent limitation of PGD as a projection-space optimizer simplifies assumptions about material responses, causing suboptimal dose control and local minima trapping. This revealed critical challenges posed to early algorithms by insufficient global optimization capabilities for complex 3D inverse problems and inadequate modeling of nonlinear material responses.

In 2020, Loterie et al. [32] implemented an integrated feedback system that regulates photopolymerization kinetics across the entire build volume, thereby improving the geometric fidelity of solidified structures. In September 2021, Bhattacharya et al. [54] developed the penalty minimization (PM) framework and compared it with the dose matching (DM) algorithm to address PGD's deficiencies by establishing constrained dose optimization. PM uses the limited-memory Broyden–Fletcher–Goldfarb–Shanno with box constraints (L-BFGS-B) optimization algorithm with dynamic penalty mechanisms for dose constraint violations, significantly improving dose uniformity. DM directly minimizes mean square errors between target and projected doses. PM is superior to DM in standard deviation and mean intersection-over-union (mIoU) metrics, particularly in suppressing over-curing and partial sedimentation. This breakthrough transformed the light-dose control vs. geometric fidelity trade-off into a constrained optimization problem, thereby laying the foundation for subsequent algorithmic development.

In December 2021, Rackson et al. [55] proposed object-space model optimization (OSMO), which reformulated the problem through algebraic modeling by maximizing the light dose contrast between target and background regions. OSMO maintained high precision under imperfect optical parameters and enabled grayscale control for functionally graded materials. Its innovation lay in shifting optimization from the projection space to the object space to address contrast attenuation from optical–chemical coupling. However, OSMO lacked explicit boundary precision handling. In June 2023, Zhang et al. [56] established edge-enhanced OSMO (EE OSMO), a dual-phase edge optimization strategy that iteratively strengthens internal edges while weakening external ones. This strategy introduces "edge error" as a new quality metric. EE OSMO outperforms OSMO in volume error rate and process window metrics, marking the evolution from global DM to localized edge refinement that resolved submillimeter feature reconstruction blurring.

In January 2023, Webber et al. [57] proposed 3D ray tracing to resolve the inherent 3D non-telecentricity in projector-based volumetric printing systems. This method demonstrated high-fidelity printing in non-telecentric configurations with extended etendue, tripling the vertical build volumes of standard Radon approaches. Furthermore, 3D ray tracing expanded the configuration possibilities of TVP for faster, cost-effective, higher-fidelity printing. In July 2023, Orth et al. [58] addressed systematic under-curing through deconvolution volumetric printing. By modeling coupled chemical diffusion and optical blurring, which is significant for features ≤0.5 mm, this method employed deconvolution-corrected dose distributions to achieve high-fidelity printing of multiscale features (e.g., fine-tooth gears), breaking resolution barriers imposed by optical diffraction and chemical diffusion while bridging the fidelity gap between volumetric printing and industrial standards. In January 2024, Chen et al. [59] proposed an expectation maximization (EM)-based framework to tackle large-volume/high-attenuation materials. Through the probabilistic modeling of light attenuation paths, this method enhanced light penetration depth in highly attenuative materials, thereby improving algorithm robustness and scenario generalization.

In April 2024, Wechsler et al. [60] mitigated resolution limitations (approximately 20 μm) under conventional ray optics assumptions by developing a rigorous wave-optical optimization framework. This approach moves away from ray optics approximations and utilizes angular spectrum plane-wave propagation modeling and memory-efficient gradient calculations to optimize 3D light fields. Simulations revealed that ray optics models produce significant artifacts for features ≤20 μm due to neglected diffraction effects [61], whereas wave-optical optimization achieved sub-20 μm resolution with full-volume consistency. This breakthrough elevated optical modeling in volumetric printing from geometric to physical optics, resolving diffraction-induced resolution limits and spatial heterogeneity while establishing theoretical foundations for holographic phase encoding. In September 2024, Li et al. [62] unified existing algorithms under an L_p-norm minimization framework, categorizing DM, PM, and OSMO as parametric instances (e.g., L_1 for sparse error penalty and L_2 for mean-square optimization). By incorporating local tolerance and weighted relaxation strategies, this framework transitioned the algorithm optimization from discrete methods to universal mathematical modeling.

In November 2024, Nicolet et al. [63] introduced a differentiable inverse rendering framework that optimizes TVP projection patterns through physical light transport modeling. This approach enables printing in arbitrary scattering resins and asymmetric containers, while overcoming voxel resolution limits via surface-aware discretization. Consequently, it achieved 4.5 times faster exposure in scattering media and near-perfect Jaccard index accuracy. In February 2025, Álvarez-Castaño et al. [64] revolutionized projection systems by developing holographic phase encoding. This technology generates low-divergence beams (Bessel/vortex) approximating Radon transform assumptions via holography [65] and high-speed digital micromirror device (DMD) control (22 kHz), achieving a 28-fold improvement in light efficiency. Combining point spread function engineering with wave-optical optimization, the proposed framework extended resolution limits toward $\lambda/(2\mathrm{NA})$ and enabled scattering-medium printing without amplitude correction, thereby resolving the co-optimization challenge between optical efficiency and dynamic control (λ is the wavelength of light source and NA is the numerical aperture of the Fourier lens).

Algorithmic evolution resulted from research efforts progressively addressing scientific challenges through optimized dimensionality expansion, constraint mechanism refinement, nonlinear inverse problem solving, multiphysics coupling modeling, resolution limit breakthroughs, and opto-mechanical-computational co-optimization. From empirical trial-and-error to model-driven approaches, and from macroscale development to micro/nanoscale precision, these advancements have significantly enhanced printing accuracy, efficiency, and material compatibility, as well as the ability to fabricate functionally graded materials. With continuous algorithmic improvements, TVP is poised to launch rapid, precise manufacturing across diverse domains, including optics, biomedicine, and microfluidics.

3 Bioinks

3.1 Bioink requirements of different bioprinting methods

Bioinks are the basic biomaterials used for bioprinting that contain cells and/or biological molecules [1, 66]. Bioprinting imposes several common requirements for bioinks, including suitable viscosity, high crosslinking rate, and favorable biocompatibility. In this subsection, we present a horizontal comparison of bioink formulations across three bioprinting methods: 3D extrusion bioprinting (EBP) (Fig. 3a), projection-based 3D bioprinting (PBBP) (Fig. 3b), and TVBP (Fig. 3c), to demonstrate an intuitive understanding of their similarities and differences, thereby facilitating smoother adjustments in ink formulations when transitioning between printing technologies.

The most common and readily accessible bioprinting method is 3D EBP [2] (Fig. 3a). Extrusion-based bioinks must satisfy extrudability requirements. Because bioinks typically require moderately high viscosity to maintain the uniform dispersion of embedded cells, extrusion bioinks must exhibit shear-thinning properties to ensure that high-viscosity bioinks transition to fluid, low-viscosity states under nozzle shear stress, enabling successful extrusion onto the printing platform [67]. Simultaneously, extrusion bioinks must possess shear recovery capability to maintain structural integrity post-deposition, which is often achieved by triggering chemical crosslinking after extrusion to stabilize the deposited structures. The morphology of extruded bioink filaments is critical for ensuring the fidelity of printed

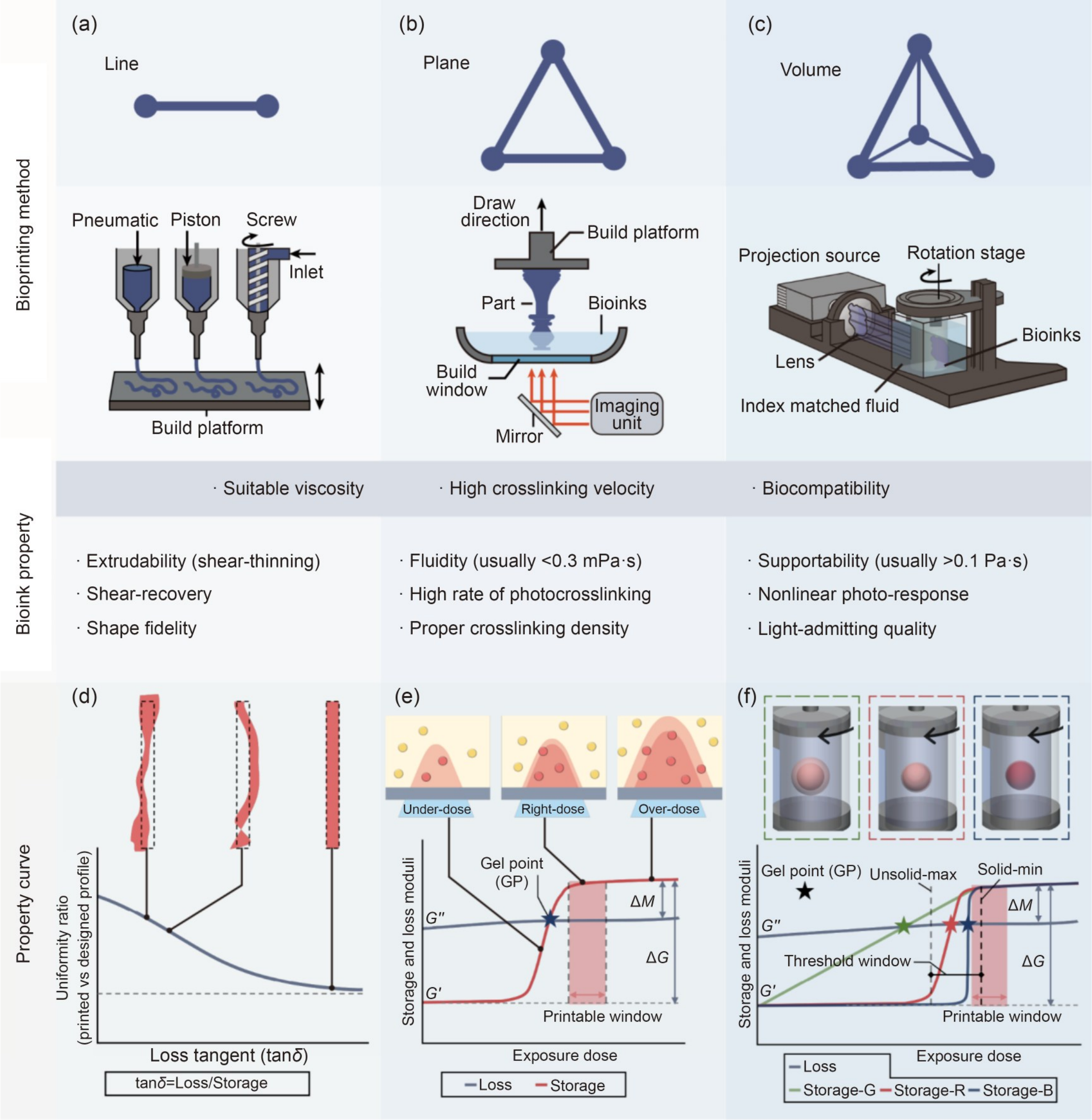

Fig. 3 Comparison of bioink design between 3D extrusion bioprinting (EBP), projection-based 3D bioprinting (PBBP), and tomographic volumetric bioprinting (TVBP). Schematic illustrations of 3D EBP (line as forming unit) (a), PBBP (plane as forming unit) (b), and TVBP (volume as forming unit) (c). Property curves of bioinks in 3D EBP (d), PBBP (e), and TVBP (f). (c) is reproduced from [19], under exclusive license to AAAS; (d) is reproduced from [69], with permission from Springer Nature Limited; (e) is reproduced from [15], with permission from Springer Nature Limited

models [68]. The uniformity of extruded bioink filaments varies with the rheological loss angle tanδ (Fig. 3d), reflecting the balance between ink fluidity and shape retention [69]. The loss angle, defined as the ratio of the loss modulus to the storage modulus, increases with enhanced fluidity, indicating progressive improvement in filament uniformity.

PBBP [15] (Fig. 3b), recognized for its exceptional resolution/time manufacturing ratio (approximately 2×10^{-3} m^2/min) [70], has become widely adopted in biomedical applications. PBBP bioinks require high fluidity (typically <0.3 mPa·s) to rapidly refill the printing area during platform movement [15]. Furthermore, PBBP bioinks must exhibit rapid crosslinking rates (ideally within seconds) to preserve cell viability and prevent material denaturation or light scattering caused by prolonged exposure. Crosslinking density is crucial for maintaining a cell-friendly microenvironment. A too-low crosslinking density (e.g., gelatin methacryloyl (GelMA) with 30% amino substitution) compromises structural integrity, whereas a too-high crosslinking density (e.g., poly(ethylene glycol) diacrylate (PEGDA)) restricts cell growth. Photorheological characterization reveals distinct curing behaviors under identical materials but varying exposure parameters [15] (Fig. 3e). Exposure parameters, such as intensity and duration, collectively determine the exposure dose (product of intensity and time), which governs the degree of crosslinking. The exposure dose window for high-resolution printing is remarkably narrow (typically <10 mJ/cm^2), with cellular components further tightening this requirement [17]. This printable window must be empirically determined through iterative trials, on various printing structures and materials. Insufficient exposure doses result in under-crosslinked layers that are too soft to support subsequent ones, whereas excessive doses cause over-curing and compromised fidelity. By establishing a crosslinking theoretical model specific to macromolecular hydrogels and analyzing their pre- and post-gelation crosslinking properties, researchers proposed a fast–slow (F–S) crosslinking strategy: rapid crosslinking (high-intensity short-term exposure) during printing, followed by slow crosslinking (low-intensity long-term exposure) post-processing. This approach enhances resolution and speed while maintaining cell viability above 90% [71].

As an emerging bioprinting technology, TVBP (Fig. 3c) imposes unique ink requirements, including moderate viscosity and optical transparency [47]. The photochemical response of materials critically influences printing fidelity [19, 62]. First, we defined a TVP-specific threshold window based on voxel-specific light dose accumulation differences induced by the global light field within the vat. The left boundary of this window is indicated by the maximum light dose in non-target regions (Unsolid-max), while the right boundary is determined by the minimum light dose in target regions (Solid-min). After computing projection images using slicing algorithms, the width of this window can be precisely determined [55]. The window shifts rightward as projection time increases, proportionally expanding with each full rotation cycle through voxel-wise light dose accumulation. Transient threshold window fluctuations caused by partial rotation cycles are disregarded. Subsequently, we examined the influence of material photochemical responses on printing. The storage modulus curve (storage-R) shown in Fig. 3f presents an ideal nonlinear response to accumulated light dose, aligning with the working curves established for PBBP. After gelation, this curve displays a suitable printable window. Furthermore, the figure demonstrates that when Solid-min reaches this window, Unsolid-max remains below the gelation point, ensuring high-fidelity printing. Insufficient printing time keeps the Solid-min below the gelation point or printable window, resulting in incomplete target region crosslinking. Excessive printing time risks the Unsolid-min surpassing the gelation point, leading to over-curing. We further considered two extreme scenarios [72]. One is near-linear photochemical responses (storage-G), where the gelation point lies far from the printable window. To achieve adequate curing, the Solid-min must reach the window, while the Unsolid-max may exceed the gelation point, causing unintended peripheral curing and fidelity loss. The second scenario is binary-like responses (storage-B), where the gelation point closely aligns with a narrow printable window. Here, non-target regions resist curing, while target regions risk over-crosslinking, thereby altering physicochemical properties. Both scenarios ultimately render these materials unsuitable for TVBP.

Although qualitative correlations between bioink properties and printability outcomes have been established in TVBP, further research is needed to develop quantitative bioink printability models. Such models will accelerate bioink development and precisely guide high-fidelity printing under diverse material formulations.

3.2 Bioink design recommendations

In volumetric curing systems, photosensitive inks primarily undergo two crosslinking mechanisms: chain-growth and step-growth polymerization [73]. Chain-growth systems [71] rely on radicals from photoinitiators to attack vinyl groups (e.g., acrylate C=C), initiating uncontrolled radical propagation where monomers are sequentially added to growing chains until termination by recombination or disproportionation. This stochastic process inherently generates network heterogeneity with uneven crosslink density, dangling chains, and loops, causing significant shrinkage stress (5%–15%) and mechanical brittleness [74, 75]. Critically, the rapid kinetic chain growth often leaves >10% of unreacted vinyl groups [76]. Residual acrylates hydrolyze into cytotoxic acrylic acid, whereas methacrylates exhibit lower reactivity but still pose biocompatibility risks [76]. Furthermore, dissolved oxygen quenches initiating or carbon-centered radicals, forming peroxyl radicals (ROO·), severely inhibiting surface and subsurface curing and degrading resolution [76, 77].

Step-growth systems [75, 78] employ precise photochemical reactions where radicals mediate stoichiometric bond formation. In thiol-ene chemistry (e.g., norbornene-thiol, vinyl ester-thiol), radicals preferentially abstract thiol hydrogen (S–H) to generate thiyl radicals (S·), which are then selectively added across “ene” bonds via step-wise chain transfer [76, 77]. This mechanism ensures homogeneous network formation governed by Flory–Stockmayer statistics, minimizing shrinkage (<2%) and evenly distributing stress for enhanced toughness [79, 80]. In thiol-ene systems, thiols scavenge oxygen to form non-inhibitory sulfonates, effectively eliminating oxygen inhibition. Although favorable for uniform curing in conventional photopolymerizations, this absence of oxygen inhibition can be detrimental in TVP, where oxygen inhibition is beneficial for spatial confinement of curing [19]. Therefore, appropriate free radical inhibitors can be integrated into the thiol-ene system to enhance its resolution in TVP [20, 36, 81]. The tyrosine photo-oxidative dimerization mechanism is a unique step-growth approach that facilitates the direct crosslinking of natural proteins without requiring chemical modification [44, 82]. Despite the requisite of dual components and higher costs, the advantages of step-growth systems in bioprinting [83, 84] should be understood. Furthermore, the choice of material systems still depends on the tradeoffs among biocompatibility, printing resolution, and the mechanical characteristics of the specific application scenario.

TVBP-specific inks often contain a biocompatible material (usually photocurable hydrogels [47, 70, 85]), a photoinitiator, and bioactive ingredients and/or cells. Furthermore, the physicochemical properties of inks critically influence printing accuracy, structural stability, and biological functionality. Bioink design must systematically address three core elements based on research advancements and practical experience (Fig. 4): high-viscosity rheological control, high-penetration optical tuning, and biocompatibility. Together, these considerations ensure the suitability of inks for complex bioprinting applications.

3.2.1 High-viscosity rheological control

Numerical models of material–property/process–parameter effects on part sedimentation demonstrate that high ink viscosity is essential for counteracting gravity-driven settling and maintaining uncured structure stability [86, 87]. Blending polymers, such as bisphenol A glycerolate diacrylate with PEGDA (7:1 ratio), achieves viscosities of (93,000± 5000) cP (1 cP=1 mPa·s), at which synergistic yield stress and storage modulus enhance anti-settling performance [19]. For biocompatibility-driven scenarios, thermoreversible physical networks (e.g., gelatin) provide temporary structural support during low-temperature printing and are subsequently removed via thermal dissociation. Sacrificial gelatin additives enable cell-compatible volumetric bioprinting of macromers based on polyethylene glycol (PEG), hyaluronic acid, and polyacrylamide [88]. Such systems prevent positional shifts during polymerization while suppressing oxygen/radical diffusion, enhancing fidelity and resolution. Gel-state printing also mitigates cell sedimentation during bioprinting [21].

Non-crosslinking polymers (e.g., 0.5% alginate (mass fraction)) exploit chain entanglement to boost the viscosity of low-molecular-weight precursors (e.g., 15% PEGDA (mass fraction)) from <1 to 50 mPa·s, enabling low-cost volumetric printing [89]. For non-biological applications, thermoplastic ethyl cellulose systems can establish physical networks with 0.1–10 kPa storage modulus and 2.7 kPa yield stress, achieving sedimentation-free tomographic patterning in low-viscosity monomers [90]. Hardware advancements, such as high-angle-dose-rate printers, demonstrate high-fidelity printing of 12 cP PEGDA [91]. This innovation shortens the curing interval by superimposing light fields from multiple light engines, thereby ignoring the influence of gravitational sedimentation and broadening the viscosity range of printable inks. SpaceCAL [92] and xolography [93] technologies demonstrate the feasibility of high-fidelity printing with 11 mPa·s inks when the traditional rheological limitation is circumvented under microgravity.

3.2.2 High-penetration optical tuning

Volumetric printing requires precise optical penetration for voxel crosslinking, necessitating ink transparency matched with optical systems. Common photocurable hydrogels like GelMA [94], hyaluronic acid methacrylate [95], and PEGDA [96] exhibit intrinsically low light scattering, ensuring accurate 3D reconstruction. According to the Beer–Lambert law, to ensure that the light intensity after traversing the entire build volume remains at least 37% (i.e., transmittance $I/I_0=1/e$), the condition $\ln(10)\varepsilon Dc=1$ must be satisfied, where ε is the molar extinction coefficient of the photoinitiator, D is the diameter of the cylindrical build volume, and c is the photoinitiator concentration. Accordingly, the photoinitiator concentration can be optimized to match the build volume dimensions and extinction coefficient.

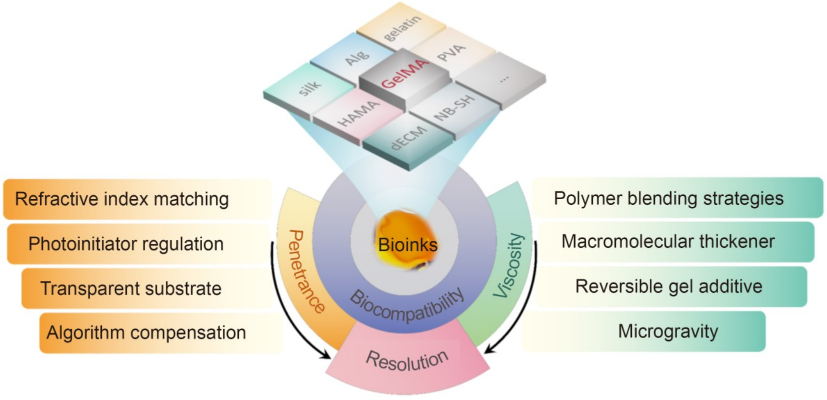

Fig. 4 Some recommendations for bioink design

Type I initiator lithium phenyl(2,4,6-trimethylbenzoyl)phosphinate (LAP) can achieve effective crosslinking at as low as 0.037% (mass fraction) [21] (typically 0.05%–0.1% (mass fraction) [97, 98]) while maintaining light penetration and reducing the cytotoxicity risk. Long-wavelength sources (e.g., green light) enhance penetration for large structures. Visible-light systems (400–500 nm, $\lambda_{\max}$=452 nm) using Ru(II)/sodium persulfate (SPS) or acylphosphine oxide Type II initiators generate Ru(III) and sulfate radicals by photolysis [99], which oxidize tyrosine residues for protein crosslinking. Based on this system, the crosslinking of bioinks, such as fibroin protein and extracellular matrix, can be achieved using visible light, expanding the scope of applicable materials for volumetric printing [44, 82, 100]. To address the scattering problem caused by cell load, the use of refractive index-matching compounds, such as iodixanol [101], which is commonly used as a contrast agent for X-ray imaging [102], can significantly reduce the scattering artifacts of subcellular components (e.g., nuclei [103]) and increase the ballistic light ratio. In practical biological applications, the appropriate amount of such additional components must be carefully controlled in the culture environment to maintain the hydrogel stability for subsequent printing [101].

3.2.3 Biocompatibility

Ink design for TVBP applications must ensure cell viability and tissue functionality. Thiol-ene click chemistry (e.g., gelatin-norbornene/thiol) enables approximately 10 s curing with nearly 100% cell viability via step-growth mechanisms, offering a tunable modulus (40–15 kPa) through substitution degree and crosslinker ratios [104]. Similarly, allyl-modified gelatin/PEG-tetrathiol systems create ultra-soft networks (0.2–1.0 kPa) for soft tissue engineering [105]. Dynamic thiol-ene polyvinyl alcohol (PVA)/gelatin systems promote cell migration and osteogenic differentiation through low polymer content and stress moderation, combined with 3D tomographic lithography for spatiotemporal control [45]. Notably, thiol-ene systems are less forgiving than chain-growth polymerization ones. Exceeding the minimal gelation dose rapidly depletes ene groups, eliminating their protective radical scavenging, which subsequently exposes encapsulated cells directly to toxic initiator-derived radicals. Decellularized extracellular matrix (dECM)-based inks used for printing via Ru/SPS systems within 30–45 s preserve native matrix components while supporting cardiomyocyte synchronization and chondrogenic differentiation [82]. Recently, a 3D model of a bionic breast duct/alveoli was printed in vitro based on mammary dECM to simulate the function of secretory mammary tissue [106].

These systematic design principles provide material scientists with innovative strategies spanning rheological control to biofunctional integration, and reveal the complex relationship among ink characteristics, printing parameters, and tissue microenvironment for medical engineers. The innovative design and use of bioinks based on these principles will advance the development of TVBP toward higher-precision and broader applications.

4 Printing resolution and efficiency

4.1 Evaluating printing resolution

Preliminary printability is assessed during printing via monitoring cameras (Fig. 5a) [32]. More accurately, the dynamic evolution of the 3D refractive index field can be monitored in real time using color schlieren imaging and tomographic reconstruction technology to meet the needs of micron-level monitoring and provide key data support for real-time feedback optimization of projection dose (Fig. 5b) [107]. After printing, macroscopic evaluation of the sample geometry is performed by visual inspection and camera imaging (Fig. 5c) [32], while microscopic features are inspected by light microscopy (Fig. 5d) [101]. Cell-laden constructs are evaluated for structural fidelity and cellular distribution by fluorescence staining combined with confocal laser scanning microscopy (Fig. 5e) [108]. Reconstructed 3D images are generated using microscope-specific software (e.g., Leica LAS X or Zeiss ZEN) or open-source tools (e.g., ImageJ) after correcting *z*-axis optical distortions [109].

For higher-precision analysis, light sheet microscopy [38, 110] (Fig. 5f) and micro-CT (Fig. 5g) [32] are used to reconstruct complete sample architectures. The shape of the sample reconstructed through open source software, such as NRecon, can also be compared with that of the original 3D model through the ImageJ plug-in or using dedicated software, such as CloudCompare. These tools calculate volumetric fidelity deviations between the printed sample and the original design, typically as percentage matches (Fig. 5h) [32]. For instance, TVBP structures generally exhibit <10% volumetric variation compared to source STL files via micro-CT analysis [21]. More intuitively, the reconstructed sample morphology can be color-coded to show its major structural size changes, such as the internal branched channel diameter (Fig. 5i) [98].

Current TVP methods exhibit varying resolutions across material systems. For positive features (e.g., filaments, overhangs), acrylate-based formulations demonstrate 80-μm-thin overhangs (e.g., Notre Dame model) at approximately 20 s [32]. The micro-CAL system can fabricate minimum characteristic size structures of 20 μm for polymers and 50 μm for fused quartz [20]. Silk fibroin bioinks optimized by Ru(II)/SPS concentration modulation (0.25 mmol/L for

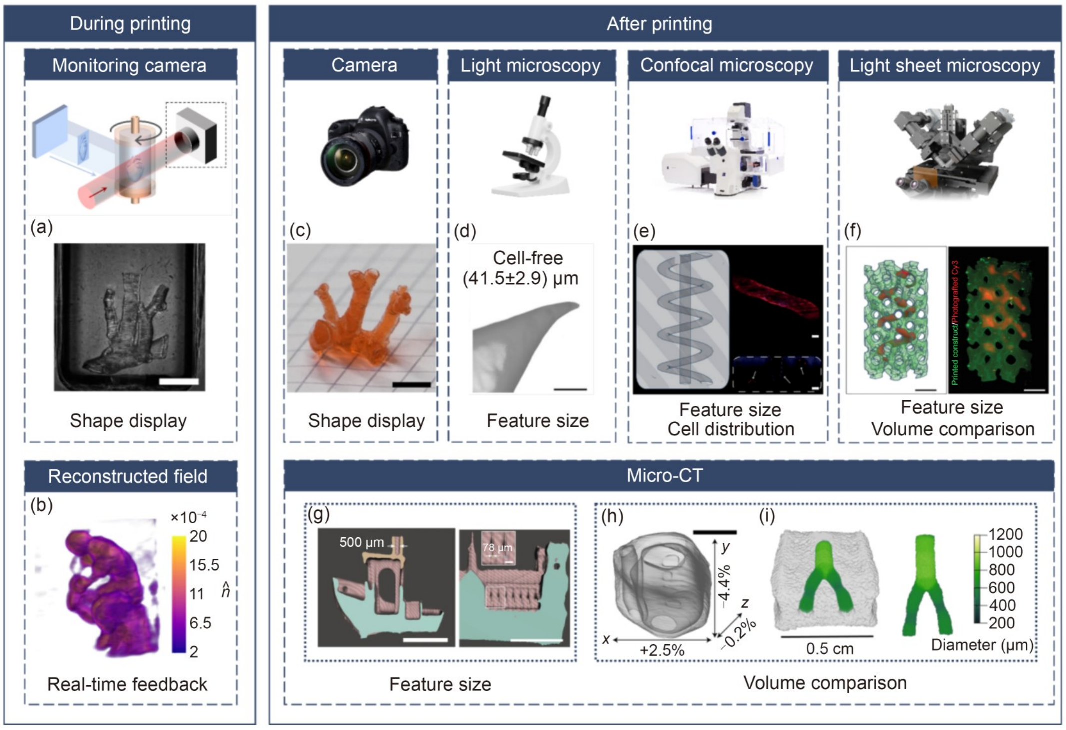

Fig. 5 Evaluation methods of printing resolution. (a) Video snapshot during the printing of the vascular artery; scale bar: 5 mm. (b) Reconstructed 3D field based on color schlieren images captured during the printing of Auguste Rodin's sculpture *The Thinker*. (c) Photograph of the printed artery perfused with a red dye, to visualize the open channels; scale bar: 5 mm. (d) Stereomicroscopy image showing the printing of a star-shaped construct, zooming in on the fine feature points of the star; scale bar: 500 μm. (e) Image of volumetrically printed constructs containing a cell monolayer in a channel taken with a confocal microscope; scale bars: 200 μm. (f) Light sheet 3D reconstruction of the printed model (green) and the photografted spiral (red); scale bars: 2 mm. (g) Micro-CT cross-section; scale bars: 5 mm (scale bar of the inset is 0.5 mm). (h) Deviation of the printed parts with respect to the original model, as measured on micro-CT; scale bar: 5 mm. (i) 3D rendering of a micro-CT scan of a branched channel model, including 3D volume reconstruction and dissected channel; green color indicates the channel diameter. (a, c, g, h) are reproduced from [32], licensed under CC BY 4.0; (b) is reproduced from [107], licensed under CC BY 4.0; (d) is reproduced from [101], licensed under CC BY; (e) is reproduced from [108], licensed under CC BY; (f) is reproduced from [38], licensed under CC BY; (i) is reproduced from [98], licensed under CC BY

Ru(II) and 2.5 mmol/L for SPS) and molecular weight regulation (88.9 kDa) attained a minimum filament thickness of 57 μm [44]. Sericin-based formulations (5% concentration) printed at 3 mW/cm^2 intensity for 30 s achieved lower line thicknesses of 45.9 μm. GelMA-poly(N-isopropylacrylamide) (pNIPAM) hydrogels achieved positive feature resolutions of (59.6±2.0) μm [108], while cell-laden systems with 0.3 g/mL iodixanol were used to print star-shaped structures at (49.2±8.4) μm [101]. For negative features (e.g., pores, channels), acrylate resins can form 500-μm-diameter hollow chimneys, while the micro-CAL system can manufacture channels with diameters and wall thicknesses as low as 150 and 85 μm, respectively [20]. GelMA-pNIPAM can achieve approximately (123.7±2.6) μm pore resolutions, with boat-model pores exhibiting a variation range of 112–170 μm. Precise replication of GelMA hollow channels (∅≤1 mm) further validates complex negative-feature feasibility [98]. Overall, current TVP technology can typically achieve resolutions of 45–80 μm for positive features and 100–500 μm for negative features.

Printed structures undergo three phases during light dose accumulation: under-curing, ideal forming, and over-curing (Fig. 6). Maintaining the dose within the optimal forming window is critical for fidelity. Current limitations in optical penetration depth and dose deposition algorithms occasionally cause defects in sharp-angled structures (e.g., Notre Dame spires), indicating the need for further investigations into resolution-limiting factors in TVP.

4.2 Optimizing printing resolution

TVBP technology resolutions are governed by the multidimensional interaction among optical system performance, bioink properties, chemical kinetic behavior, and algorithm optimization capabilities (Fig. 7). The subsequent discussion will elaborate on these four aspects by analyzing prior studies.

4.2.1 Optical system performance

The optical system configuration for TVBP typically comprises two modules: a projection printing module and a

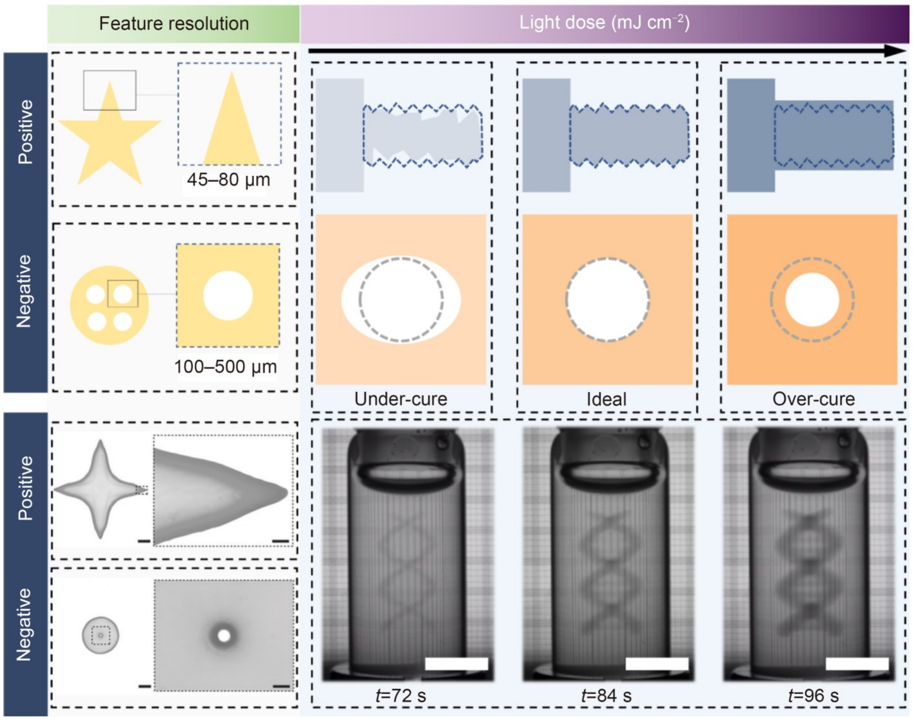

Fig. 6 Schematics of feature resolution and three curing stages, with the corresponding printed objects. Part (the positive and negative features in the bottom left) is reproduced from [108], licensed under CC BY

monitoring module. The projection printing module generally consists of an input laser source, optical lenses, a spatial light modulator (SLM) [64]—usually implemented as DMDs [111, 112] (i.e., an array of microscopic mirrors that individually tilt to adjust light intensity), which have evolved from commercial projection displays to become a key component in high-speed, maskless optical patterning systems (e.g., TVBP)—a 4f system, a refractive index-matched square vat, and a rotating resin-containing vial. The monitoring module includes an orthogonally aligned illumination laser source, optical lenses, and a monitoring camera. The optical system is physically limited by the fundamental constraints on resolution. The projection resolution of DMD (acting as a dynamic mask) directly determines the theoretical minimum feature size (e.g., effective pixel size, 22.8 μm [21]), while the wavelength selection of the light source (e.g., 405 nm [21], 525 nm [44]) influences the penetration depth and scattering losses of the light field (Fig. 8a). Etendue and depth-of-focus parameters further limit imaging quality at the edges of the build volume [32] (Fig. 8b). Etendue, mathematically defined as the product of the area and solid angle, is a fundamental property of optical systems that governs the number of light rays passing through the system. Etendue is expressed as Eq. (5) [113, 114]:

$$\text{Etendue}=\pi\cdot A\cdot \text{NA}^2, \tag{5}$$

where A is the cross-sectional area of the flux, $\pi\cdot\text{NA}^2$ is the radiometric solid angle, and $\text{NA}=\sin\theta$ (here θ denotes the maximum incident angle of light). Away from the center of the build volume, the effective pixel size increases proportionally to the divergence of the illumination beam. To constrain the fractional overlap (p) between pixels at the build region edges, ray-optical analysis of the projection system yields Eq. (6) [32]:

$$L_{\text{S}}\cdot\text{NA}_{\text{S}}=n\cdot p\cdot L_{\text{vox}}, \tag{6}$$

where L_{S} is the spatial extent of the illumination source, NA_{S} is the numerical aperture of the source, n is the refractive index of resin, and L_{vox} is the voxel resolution in the center of the build volume. Loterie et al. [32] coupled six laser diodes into a square-core fiber (L_{S}=70 μm, NA_{S}=0.22) to achieve a theoretical optical resolution of 23 μm at the center of a 16 mm×20 mm build volume, with the experimental edge resolution degrading to 33 μm [32]. This phenomenon is particularly pronounced in non-telecentric optical systems, demonstrating that TVP resolution is etendue-limited rather than diffraction-limited. Furthermore, optimization of the source etendue maximizes the utilization of the spatial frequency range achievable by DLP modulators within the build space. A “micro-CAL” [20] apparatus was constructed by coupling a laser light source with an optical fiber with a small-mode field size and low numerical aperture to demagnify the light pattern defined by the DMD. This design minimized system etendue, thereby reducing light divergence and blurring [32]. Optical resolution was measured via the modulation transfer

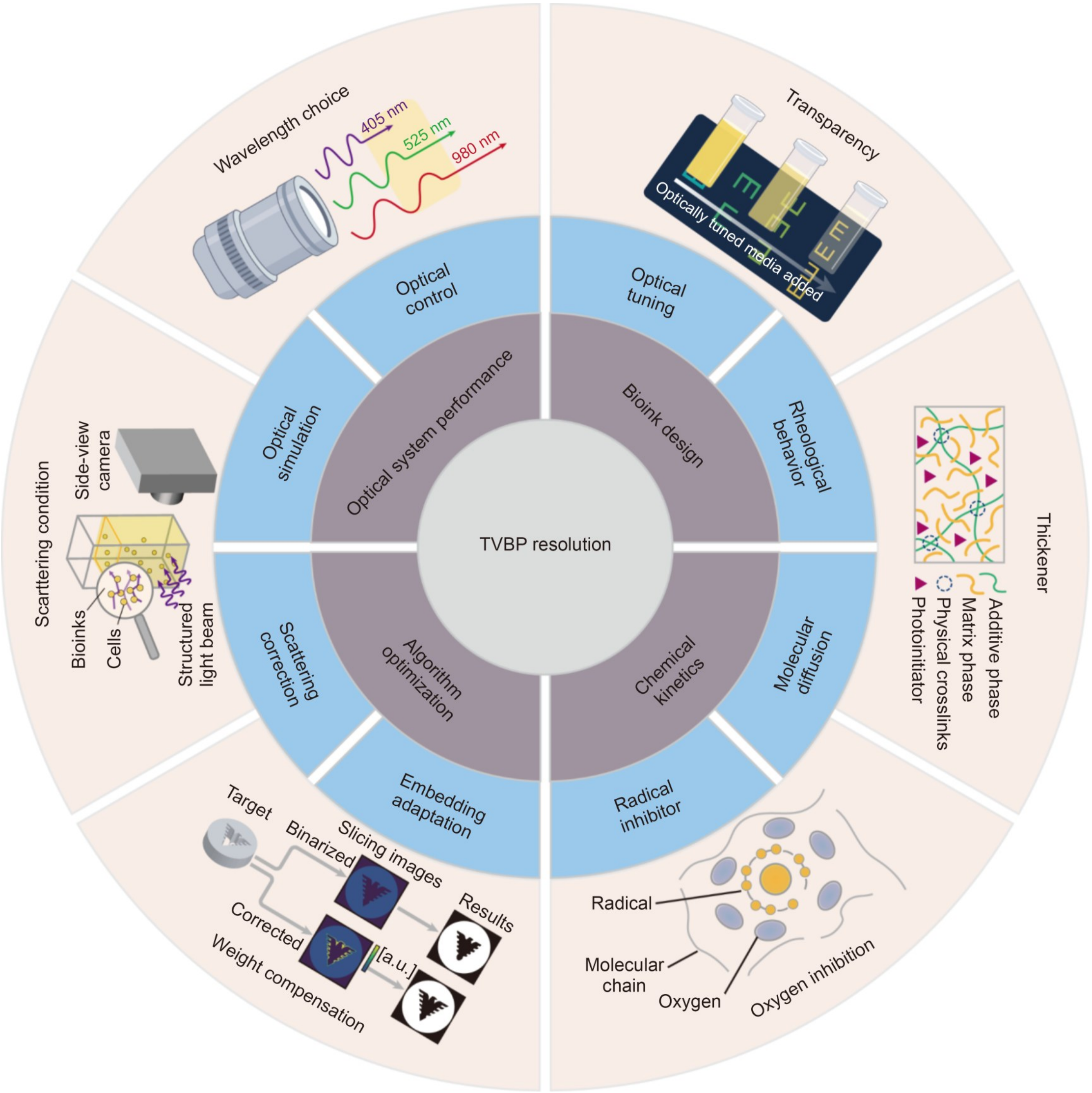

Fig. 7 Four aspects affecting printing resolution

function (MTF), achieving MTF>0.4 at spatial frequencies ≥66.7 cycles/mm in the central 1.5-mm diameter of the build volume. The micro-CAL system integrated with gradient descent digital mask optimization [19] facilitated the rapid printing (within approximately 30–90 s) of microstructures with minimum feature sizes of 20 μm for polymers and 50 μm for fused silica glass [20].

TVBP forms internal light fields through the projection of light penetration into the printing container, thereby requiring a precise understanding of light propagation paths within the printing vial. Commercial projectors typically employ non-telecentric optical paths where rays emerge from the pixel array at the left-hand side of the image, pass through an idealized projection lens (depicted as a double-sided arrow), and transmit to the photopolymerizable resin-containing vial (Fig. 8c) [57]. The cylindrical vial geometry induces strong refraction in the *XY*-plane, focusing chief rays onto the optical axis. Furthermore, rotational asymmetry of the cylindrical vial introduces astigmatism, creating distinct focal planes in sagittal and tangential planes, visually manifested as differing focal positions on the *XY* and *YZ* planes. In contrast, ray calculations using the Radon transform during slicing consider only chief rays and remain valid exclusively for low-etendue light sources (Fig. 8d) [57]. Furthermore, line integral computation along parallel paths is a fundamental requirement of the central slice theorem, necessitating telecentric approximation of rays in the *ZY*-plane (flattened rays shown in the figure). Figure 8e illustrates a telecentric projection system (DMD micromirror pitch: 10.8 μm), with its original projection lens replaced with a telecentric optical system [57]. Key components include a DMD chip serving as a pixel source and two plano-spherical lenses with an intermediate aperture. This optical design achieves a dual telecentric architecture

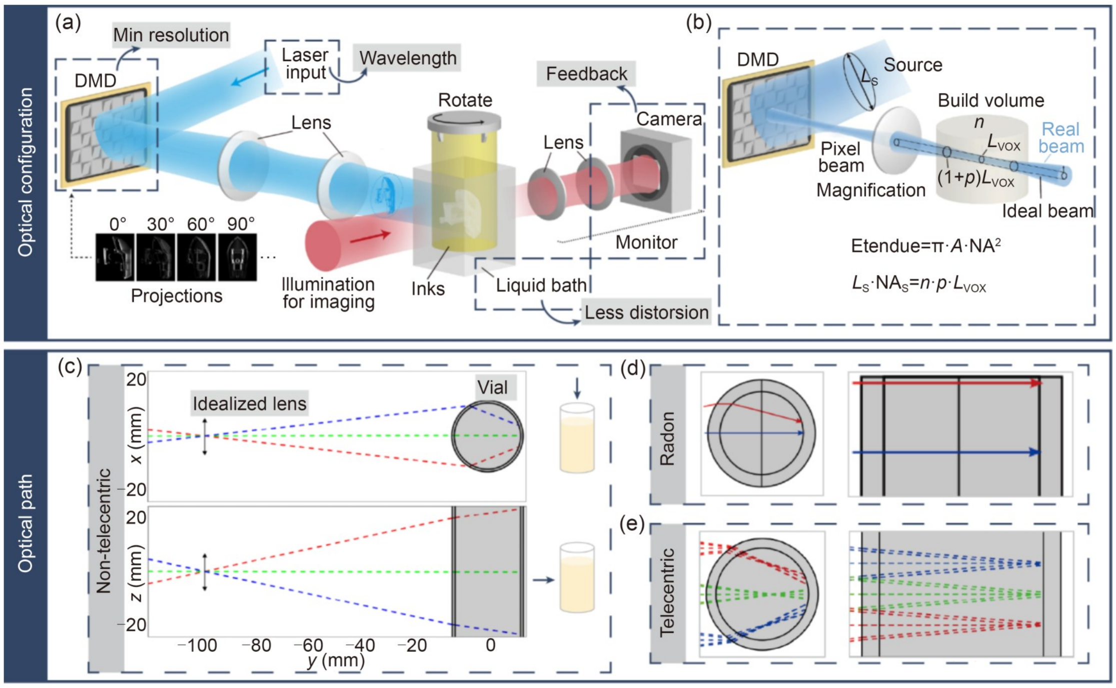

Fig. 8 Optimizing printing resolution through optical system performance. (a) Experimental setup for high-resolution tomographic printing. (b) Etendue-limited optical resolution. (c) Ray paths in the non-telecentric volumetric printer for elevation and plan views. (d) Ray paths within the vial in the *XY* and *YZ* planes using the Radon method. (e) Ray paths within the vial in the *XY* and *YZ* planes for a tomographic printer with a telecentric projection system. A is the cross-sectional area of the flux, $\pi\cdot\mathrm{NA}^2$ is the radiometric solid angle, and $\mathrm{NA}=\sin\theta$. L_S is the spatial extent of the illumination source, NA_S is the numerical aperture of the source, n is the refractive index of resin, p is the fractional overlap, and L_{vox} is the voxel resolution in the center of the build volume. (a, b) are reproduced from [32], licensed under CC BY 4.0; (c–e) are reproduced from [57], with permission from Optica Publishing Group under the terms of the Optica Open Access Publishing Agreement

with unity magnification (M=1), ensuring precise correspondence between imaging pixel size and DMD physical pitch (10.8 μm). Purely from the perspective of optical path design, such telecentric systems more sufficiently satisfy the assumptions of projection slicing algorithms than conventional non-telecentric systems, thereby facilitating high-fidelity volumetric printing.

Moran et al. [115] used a commercial ray-tracing software to examine the optical effects of cylindrical lensing imparted by a vial without index-bath immersion and another in an index-matching immersion, and evaluated the design of a negative lens to compensate for the cylindrical vial lensing. Although images near the vial center provide reasonable estimates of average exposure, print formation relies on cumulative light field integration throughout the vial. Consequently, image planes before and behind the focal plane critically influence model fidelity. Evidently, using an index-matching fluid-filled vat or a negative lens matched to the vial diameter effectively mitigates optical distortions caused by air–vial interface refraction. Therefore, when constructing models near vial peripheries, a negative lens should be employed to correct resin-vial lensing effects, which may be more convenient than employing index-matching fluid baths. Recent studies have proposed combining ray tracing with algorithmic corrections to address optical distortions caused by non-telecentricity and air–vial interface refraction, thereby reducing system complexity while achieving cost-effective high-fidelity printing [57, 116].

4.2.2 Bioink design

The practical efficacy of light field propagation critically depends on the optical and rheological properties of the ink. For TVP, the photochemical response of the ink is particularly crucial. Materials with linear responses exhibit significant blurring in reconstructed projections, demonstrating substantially higher overall response errors than nonlinear response materials (Fig. 9a) [62]. In the case of nonlinear logistic responses (Fig. 9b), superior projection reconstruction accuracy may arise from saturation regions at both ends of the response curve, rendering the ink material insensitive to certain dose variations, thereby generating a broader adjustable curing threshold range. Notably, steeper slopes in the response curve of nonlinear materials do not universally improve performance. When approaching verticality (i.e., step-function-like responses), increased errors occur in regions with intermediate target response values. Such quasi-binary response materials are more suitable for binary targets (1-bit depth), whereas for grayscale targets, appropriately reducing the response curve slope in nonlinear materials yields optimal solutions.

Furthermore, the rheological properties of inks critically influence printing fidelity. Sacrificial gelatin addition enables printing under gelled conditions, effectively preventing gravitational settling during polymerization and significantly enhancing structural fidelity (Fig. 9c) [88]. Furthermore, gel-state printing mitigates cell sedimentation in biomanufacturing processes involving cellular encapsulation [21]. Salajeghe et al. [87] investigated numerical simulations comparing flow behavior and settling of cured components in Newtonian vs. Bingham model fluids (Fig. 9d). The Newtonian fluid case exhibited pronounced settling-induced deformation, which is attributed to its higher velocity gradients and shear rates than those of Bingham fluids. In both scenarios, maximum shear rates localize around sinking components due to downward fluid motion driven by part sedimentation, which necessitates compensatory upward flows in adjacent regions to maintain continuity. Subsequently, high-shear transition zones are generated between descending and ascending flow domains. When encapsulating cells within inks, unique light scattering signatures from cells and subcellular structures create optical challenges, where the scattering mean free path is inversely proportional to cell density [117]. High cell densities induce ballistic photon attenuation and multiple scattering. These not only blur tomographic projections but also promote off-target polymerization through unintended light dose accumulation while simultaneously limiting maximum printable dimensions. Bernal et al. [101] achieved resolution

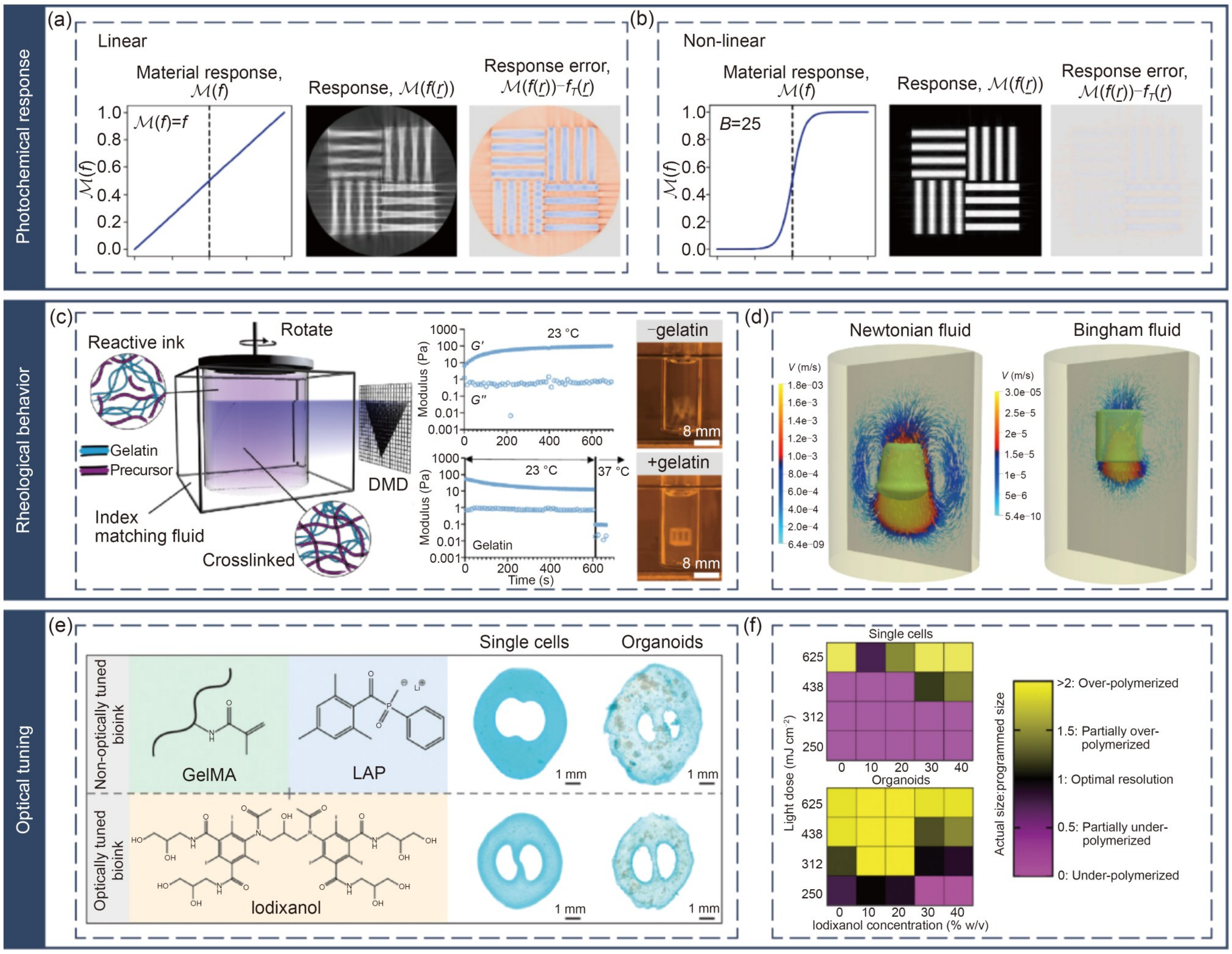

Fig. 9 Optimizing printing resolution through the bioink design. (a) Linear material response. (b) Generalized logistic function with *B*=25. From left to right, the columns are the plot of material response, response from tomographically reconstructed dose, and response error from the target. (c) Schematic of the volumetric printing of non-viscous reactive macromers using gelatin as a sacrificial material to modulate viscosity. (d) Numerical simulations comparing flow behavior and settling of cured components in Newtonian vs. Bingham model fluids, where green regions indicate cured phases while arrows depict velocity fields. (e) Enhancing TVBP of single cells and hepatic organoids through bioink optical tuning with iodixanol. (f) Printability window of 5×10^6 mL^{-1} single cells and organoids represented by the ratio of the printed fine-feature thickness to the programmed thickness. (a, b) are reproduced from [62], with permission from the authors; (c) is reproduced from [88], with permission from Wiley-VCH GmbH; (d) is reproduced from [87], licensed under CC BY 4.0; (e, f) are reproduced from [101], licensed under CC BY

enhancement through optical tuning via iodixanol addition in single-cell and liver organoid-laden bioinks (Fig. 9e). Concentration-dependent refractive index modulation increased values from 1.352 in pure GelMA to 1.3783 at 0.4 g/mL iodixanol loading. Experimental optimization was achieved with 0.3 g/mL iodixanol for hepatocyte printing and 0.1 g/mL for organoid systems, which produced 50-μm-scale features even at 1.5×10^7 cells/mL density (Fig. 9f). Notably, the universal applicability of this optical tuning strategy requires cell type-specific optimization of concentration windows. As a temporary additive, iodixanol gradually diffuses after crosslinking, with sol fraction tests showing concentration-dependent leaching rates. Considering the culture environment stability, 0.1 g/mL iodixanol was determined as the optimal concentration for organoid printing. This optimized protocol enables rapid (20 s) fabrication of intricate 3D helical structures unachievable through conventional extrusion methods, establishing novel pathways for precision manufacturing in soft tissue engineering.

4.2.3 Chemical kinetics

Spatiotemporal control of chemical kinetics is one of the core challenges for resolution enhancement. In TVP technology, radical inhibition mechanisms are essential for achieving high-precision spatial control. Unlike conventional layer-by-layer photopolymerization, TVP enables rapid fabrication through global light field construction, thereby requiring photoresponsive materials to produce pronounced nonlinear response characteristics and confine polymerization to target regions. While nonlinearity is inherent in photoresponsive materials due to gelation thresholds, this alone is insufficient for the precise manufacturing of complex 3D structures. Radical inhibitors are critical for enhancing nonlinear responses by modulating polymerization kinetic threshold behaviors. Molecular oxygen, the most ubiquitous natural inhibitor [118], forms stable intermediates through reactions with (meth)acrylate radicals as demonstrated by the photolysis of Type I photoinitiators and subsequent oxygen interactions in Fig. 10a. However, not all photopolymerization systems exhibit oxygen inhibition. A notable exception is thiol-ene polymerization, which attracts significant attention due to its click-like reaction characteristics, homogeneous network topology, and highly tunable crosslinking behavior. In this system, thiols protonate and transfer peroxy radicals back to polymer chains, counteracting oxygen inhibition. For such systems, synthetic inhibitors, such as 2,2,6,6-tetramethylpiperidinyloxy (TEMPO), effectively establish controlled threshold behaviors [20, 36], significantly improving printing resolution and edge definition (Fig. 10b) [81]. Cubic lattice structures printed with TEMPO demonstrate enhanced fidelity (Fig. 10c) [20]. Increased TEMPO concentrations further reduce overcuring in peripheral regions and internal void/gap areas. The comprehensive framework developed by Thijssen et al. [81] elucidates the mechanistic role of TEMPO as a radical inhibitor in thiol-ene systems, uncovering critical theoretical foundations for volumetric printing. Figure 10d correlates the photorheological analyses of TEMPO-containing resins with accumulated light dose distributions, demonstrating that TEMPO shifts the storage modulus (G') increase toward higher doses by introducing an inhibition period. Radical polymerization kinetics are governed by inhibitor concentration. Furthermore, the interactions between inhibitors and crosslinking systems can be quantified through phototheology and FT infrared spectroscopy to predict optimal exposure parameters and reduce trial-and-error costs.

The effects of molecular inhibition, such as oxygen inhibition, during continuous exposure may blur dose distributions through gradient diffusion, necessitating synergistic suppression via high-viscosity resins and real-time molecular monitoring. High-viscosity resins (e.g., 10 Pa·s) inhibit oxygen diffusion (diffusion coefficient $D=1.2\times10^{-13}$ $\mathrm{m^2/s}$) by restricting oxygen transport distances to below 2 μm during 20-s printing cycles to maintain spatial dose accuracy [32]. Virtual volumetric additive manufacturing (VirtualVAM) [119] simulations demonstrate the critical balance between reaction and diffusion rates in volumetric printing (Fig. 10e). Rapid radical consumption of dissolved oxygen creates concentration gradients that drive oxygen replenishment, with mass transfer efficiency governed by the Damköhler number (Da, dimensionless ratio of polymerization to diffusion rates), which directly influences feature resolution. High-Da systems (reaction-dominated) preserve sharp edges but exacerbate local conversion inhomogeneity, whereas low-Da systems (diffusion-dominated) promote global oxygen redistribution at the cost of feature rounding and microstructural loss, reflecting competitive oxygen diffusion–polymerization dynamics. Spatially heterogeneous dose distributions induced by inhibitor diffusion further constrain the concurrent fabrication of multiscale complex structures, underscoring the importance of optimized oxygen transport to balance edge precision and bulk homogeneity. Although exothermic polymerization may disrupt reaction kinetics, experimental thermal dissipation effectively mitigates temperature-induced mass transfer interference under standard conditions (Fig. 10f). This oxygen-mediated spatiotemporal equilibrium provides a chemical kinetic framework for understanding resolution limits in photopolymerization systems.

4.2.4 Algorithm optimization

In Sect. 2, we systematically summarized recent advancements in algorithmic optimization. Building upon the foundational dose optimization algorithms (e.g., PGD [19],

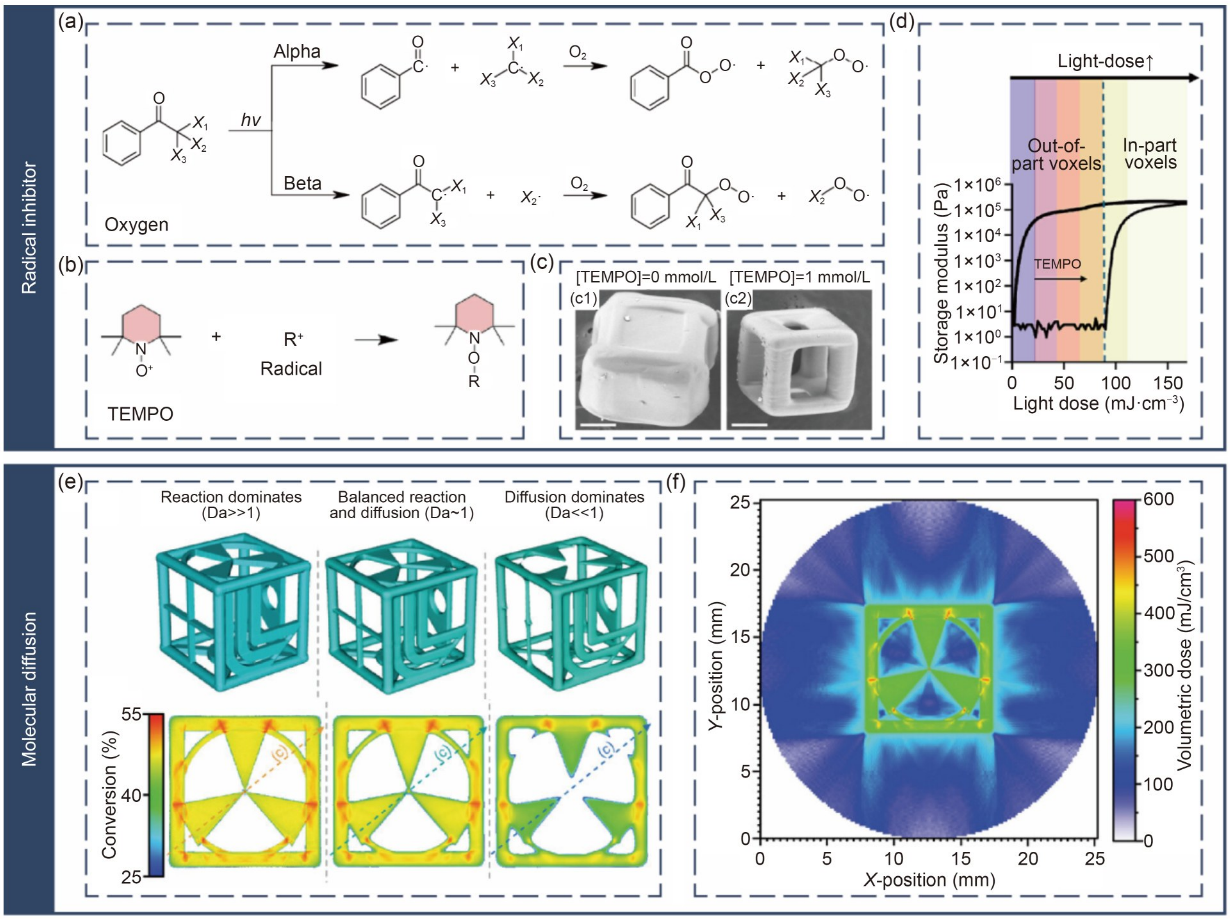

Fig. 10 Optimizing printing resolution via chemical kinetics. (a) Photocleavage of Type I photoinitiators and subsequent reaction with molecular oxygen. (b) Chemical structures and reactions involved in the thiol-ene photo-crosslinkable photoresist, consisting of multiple photoinitiators. TEMPO acts as a radical scavenger and induces a nonlinear dose response by reacting with photogenerated radicals to form stable bonds, inhibiting further polymerization. (c) Scanning electron micrographs of cube cages printed and developed with 0 and 1 mmol/L TEMPO; scale bars: 200 μm. (d) Illustration of the correlation between the photorheological analysis of the photoresist with TEMPO and the accumulated light dose distribution in volumetric printing. (e) Simulation demonstrating the importance of reaction and diffusion rates in volumetric printing. Twenty-four percent of conversion iso-surfaces for simulations proceed under reaction-controlled, balanced-reaction-and-diffusion, and diffusion-controlled conditions. (f) Heat map of the volumetric dose for the prints shown in (e). (a) is reproduced from [118], with permission from the American Chemical Society; (b, d) are reproduced from [81], with permission from Elsevier B.V.; (c) is reproduced from [20], under exclusive license to AAAS; (e, f) are reproduced from [119], licensed under CC BY-NC-ND

PM [54]), the field rapidly evolved to incorporate sophisticated feedback and correction mechanisms addressing critical limitations [32]. Object-space formulations, such as OSMO [55] and EE OSMO [56], have shifted the focus toward contrast optimization and explicit boundary precision control using iterative refinement and dedicated error metrics. Concurrently, advanced modeling techniques have been developed to tackle physical constraints: deconvolution methods [58] have corrected for coupled optical blurring and chemical diffusion; wave-optical optimization [60] have overcome diffraction limits inherent in ray optics; and EM [59] and differentiable inverse rendering [63] have mitigated complex light transport in scattering media. This technological progression, which culminates in unified frameworks (L_p-norm [62]) and hardware-aware co-optimization (holographic encoding [64]), demonstrates a clear trajectory toward increasingly robust, feedback-driven algorithms for error correction, resolution enhancement, and generalization across diverse TVBP scenarios.

Here, we further explore several optimized algorithm simulations and elucidate the critical role of simulation-driven dynamic compensation in resolution enhancement. Exposure duration, as a key control variable in TVP, typically only achieves order-of-magnitude prediction accuracy in dose calculations [119], compelling operator-dependent manual termination through visual monitoring of refractive index changes during practical printing. A proposed in situ 3D refractive index monitoring system [107] tracks local material conversion via the tomographic reconstruction of color schlieren images to successfully reconstruct evolving-phase objects within resin while validating reconstruction quality through comparisons by iso-surface laser scanning. This approach improves printing fidelity and reduces the manual iteration time for new material testing. Another automated exposure system [120] employing real-time light scattering data processing generates accurate and reproducible prints without human intervention, significantly mitigating subjective timing errors and enhancing printing fidelity/reproducibility to commercial-grade standards. However, gelation monitoring based solely on refractive index or scattering changes is limited in low-refractive-index resins (e.g., silicones, specific hydrogels) and strong dark-curing systems. It also fails to capture dynamic processes, such as radical-dissolved oxygen diffusion, which impact microstructural fidelity [121]. These predictive inadequacies significantly limit the widespread adoption of TVBP.

The VirtualVAM simulation framework can generate spatiotemporal datasets for given tomographic printing parameters, enabling the investigation of experimentally inaccessible aspects, such as single-voxel conversion curves, molecular oxygen effects, and optimal termination timing [119] (Fig. 11a). Through single-voxel reaction–diffusion modeling, exposure patterns can be optimized to enhance dose contrast. Experimental validations in Fig. 11b demonstrate the model's precise prediction of gelation initiation sites and propagation paths, which enable the monitoring of printing progression and reveal the optimal termination points. This framework provides essential theoretical tools for deciphering multi-scale interactions in volumetric printing and accelerating technological commercialization.

In TVBP, the incorporation of dispersed media (e.g., cells) requires optical tuning (as discussed in Sect. 4.2.2) to enhance overall light transmittance. Algorithmic scattering corrections could also improve printability in opaque bioinks. The correction efficacy is governed by scatterer concentration, morphology, size, and refractive index. This optical characterization method employs a DMD to project incoherent narrowband light patterns for enhanced optical sectioning contrast while capturing dynamic light propagation behavior through scattering resin, as captured via a side-view camera (Fig. 11c). Frequency-domain analysis reveals that scattering media act as low-pass filters, causing significant attenuation of high-spatial-frequency signals with depth. To address this, multi-group spatial frequency patterns (e.g., Radon transforms or stochastic patterns) are projected and combined with spectral transmission data across depths to construct correction masks that compensate for the high-frequency losses. This strategy significantly improves radial penetration accuracy by applying incident-to-attenuated spectral ratios to target dose calculations. Experimental validation using pentaacrylate/TiO_2 nanoparticle composite resin revealed that scattering correction increased gear structure intersection-over-union (IoU) from 0.56 to 0.80, which approaches transparent resin benchmarks (IoU=0.83), while preventing the over-polymerization of external gears (Fig. 11d). In bioprinting applications, this method achieved centimeter-scale cell-laden hydrogel constructs with open channels through spatial dose redistribution. It preserved the total light dose ((19.1±5.2) mJ/cm^2), printing duration (36 s), and post-printing cell viability. Although limited to ballistic photon projections in multiple scattering media, its effectiveness in weakly scattering systems (e.g., high-cell-density hydrogels) offers new pathways for balancing speed, low photoinitiator usage, and biocompatibility, expanding the potential of TVBP in functional materials and biofabrication.

Embedded object overprinting is a unique advantage of TVP. However, light occlusion from inserts significantly distorts light fields, inducing artifacts that degrade dimensional accuracy and homogeneity. Bagheri et al. [122] addressed this issue by proposing a model-weighting method (Fig. 11e) that established an in-part fidelity (IPF) metric to systematically evaluate insert-induced dose variations. Their weighted projection algorithm demonstrated 15%–67% intra-voxel dose optimization in non-convex insert models while reducing error-correction iterations. Furthermore, the IPF voxels of the weighted model exhibited a more solid structure than the unweighted model (Fig. 11f). Florczak et al. [123] integrated light sheet imaging with OSMO to implement in situ 3D occlusion mapping and dynamic light-field optimization. Validation through pillar arrays and sphere-in-cage models showed that this approach improved crosslinking uniformity and multidirectional occlusion correction. These studies improve printing quality control in complex occlusion scenarios through the complementary strategies of real-time sensing with adaptive light modulation and dose modeling/assessment innovation, thereby collectively producing multi-scale solutions to shadow artifact suppression in high-precision tomographic printing.

Multifactorial co-optimization has become the inevitable path for surpassing resolution limits. For instance, combined refractive index matching and scattering correction [41] enhances feature fidelity through physical (reduced scattering) and computational (artifact compensation) synergies. High-viscosity resins coupled with feedback optimization algorithms achieve precise fabrication of positive (80 μm) and negative (500 μm) features by suppressing oxygen diffusion and compensating for optical distortion [32]. These cases demonstrate that resolution breakthroughs must transcend single-factor optimization through optical–material–chemical-algorithmic co-design to establish adaptive printing systems.

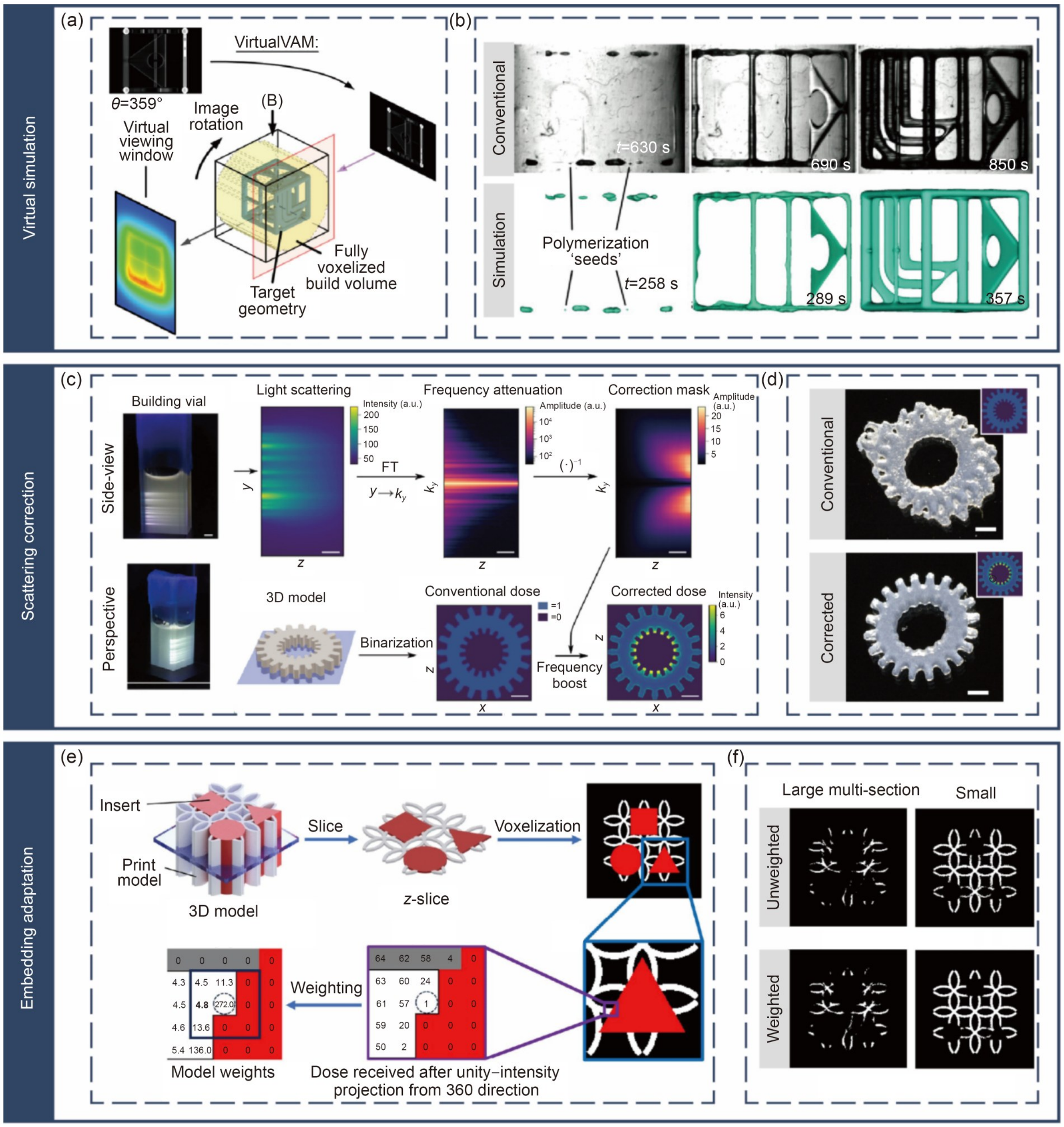

Fig. 11 Optimizing printing resolution by algorithm optimization. (a) Schematic of the VirtualVAM simulation framework with associated CT projections, illustrative geometry, and data extraction. (b) Shadowgraph images captured for a single angle showing the progression of gelation during a volumetric print (comparison with the simulation process in green color). (c) Light scattering was first characterized and then corrected; scale bars: 2 mm. (d) Comparison of printed gear models before and after correction; scale bars: 2 mm. (e) Voxelization, the dose received after unity–intensity projections and weighting in insert-caused occlusion cases. (f) In-part voxels with dose over the highest out-of-part dose under the highest-quality conditions. Top row: non-weighted models; bottom row: weighted models. (a, b) are reproduced from [119], licensed under CC BY-NC-ND; (c, d) are reproduced from [41], licensed under CC BY; (e, f) are reproduced from [122], licensed under CC BY 4.0

4.3 Improving printing efficiency

TVBP demonstrates significant efficiency advantages through its innovative harnessing of the inherent capability of light to initiate photochemical reactions throughout material volumes. In terms of photonic utilization efficiency, Thijssen et al. [124] proposed the reconceptualization of the capacity of light to drive photochemical processes uniformly through a material's entire volume (Fig. 12a). Their approach implements photochemical action spectra for optimal wavelength selection, specifically through red-shifted illumination (e.g., 470 nm) beyond the photoinitiator's absorption peaks. Wavelength optimization reduced molar absorptivity to 0.713 L/(mol·cm) while maintaining high

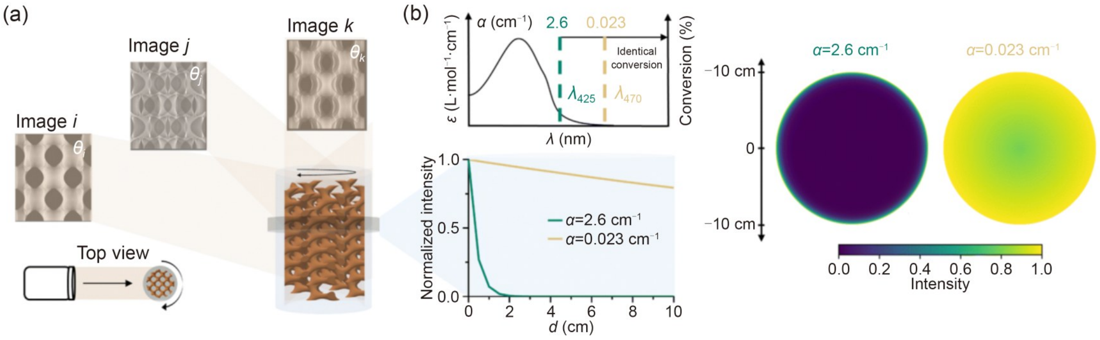

Fig. 12 Optimizing printing efficiency via photochemistry. (a) Schematic showing volumetric printing where a set of projections is delivered to a rotating photoresist volume. (b) Practical example of how red-shifting the irradiation wavelength beyond the absorption maximum can improve penetration depth and uniformity of the light dose in TVP, based on the photopolymerization of a (meth)acrylate-based resist. Reproduced from [124], with permission from The Royal Society of Chemistry

reactivity. At 0.5% photoinitiator concentration (mass fraction), the absorption coefficients decreased, from 2.6 cm^{-1} at 425 nm to 0.023 cm^{-1} at 470 nm, and were accompanied by marked improvements in light intensity distribution uniformity (Fig. 12b). Such photochemical modulation facilitates scalability from traditional 4-cm-diameter prints to 20-cm-scale objects while preserving submillimeter precision. Integrating wavelength-resolved photochemistry into volumetric printing not only enhances light uniformity and resolution but also overcomes limitations imposed by maximum absorption, thereby enabling the printing of larger and more accurate 3D structures. Álvarez-Castaño et al. [64, 125] recently revolutionized photonic efficiency through holographic phase encoding, which generated low-divergence beams (Bessel/vortex beams) approximating Radon transform ray optics. By combining it with DMD (or other SLM) high-speed temporal control (22-kHz frame rate), this approach achieved a 28-fold improvement in photonic efficiency.

In terms of time efficiency, volumetric printing presents spatiotemporal characteristics fundamentally distinct from traditional additive manufacturing methods. A study on anatomical auricle model fabrication demonstrated that all printed objects within the volume range of 0.15–4.14 cm^3 can be completed within a fixed time (22.7 s) [21]. This finding sharply contrasts with the conditions of 3D EBP, in which time increases exponentially with volume, and PBBP, in which time linearly correlates with height. Therefore, what factors limit the time efficiency of volumetric printing? Further investigations must be made into the influence on model reconstruction quality of the number of projection patterns at different angles during projection slicing generation, specifically, the angular sampling number N_θ. According to the angular sampling theorem, the angular sampling number should satisfy $N_\theta \geq \pi N_r/2$, where N_r is the spatial sampling number within the field of view. If the angular sampling number is insufficient, it will cause spatial aliasing, manifesting as artifacts or distortions in reconstructed images. Conversely, a higher angular sampling number enables denser coverage of frequency space, thereby improving reconstruction quality. The rotational speed of the vial satisfies $\omega \leq 2\pi f_p/N_\theta$, where f_p is the frame rate of the projection system. Therefore, a higher frame rate of the projection system combined with appropriate angular sampling numbers facilitates enhanced time efficiency in volumetric printing.

As shown in Fig. 13, we adopted three printing methods to print three cylindrical models of different sizes to visually demonstrate the differences in time efficiency. Figure 13a shows TVBP performed with the EFL-BP9601 printer (Yongqinquan Intelligent Equipment Co., Ltd., Suzhou, China). The process was performed using a commonly used 0.05 g/mL GelMA + 0.05 g/mL PEGDA bioink combination to print three cylindrical models: 4 mm× 4 mm (diameter×height), 8 mm×4 mm (diameter×height), and 8 mm×8 mm (diameter×height) (Fig. 13b). The printing time was only 24 s regardless of model cross-sectional area and height variations (Fig. 13c). Figure 13d shows 3D EBP using the printer (EFL-BP6601, Yongqinquan Intelligent Equipment Co., Ltd.) with a 10% (0.1 g/mL) GelMA bioink formulation to print three cylindrical models of different sizes (Fig. 13e). It can be observed that as model cross-sectional area and height increase, the time required for extrusion printing proportionally increases (Fig. 13f). Figure 13g shows PBBP using the printer (EFL-BP8601, Yongqinquan Intelligent Equipment Co., Ltd.) with a 5% (0.05 g/mL) GelMA + 5% (0.05 g/mL) PEGDA bioink combination to print three cylindrical models (Fig. 13h). It can be seen that the PBBP time consumption remains unchanged with cross-sectional area but proportionally increases with model height (Fig. 13i). This time constancy in TVBP originates from the spatially parallel characteristics of its printing process. The total manufacturing time depends solely on the kinetic process of photopolymerization

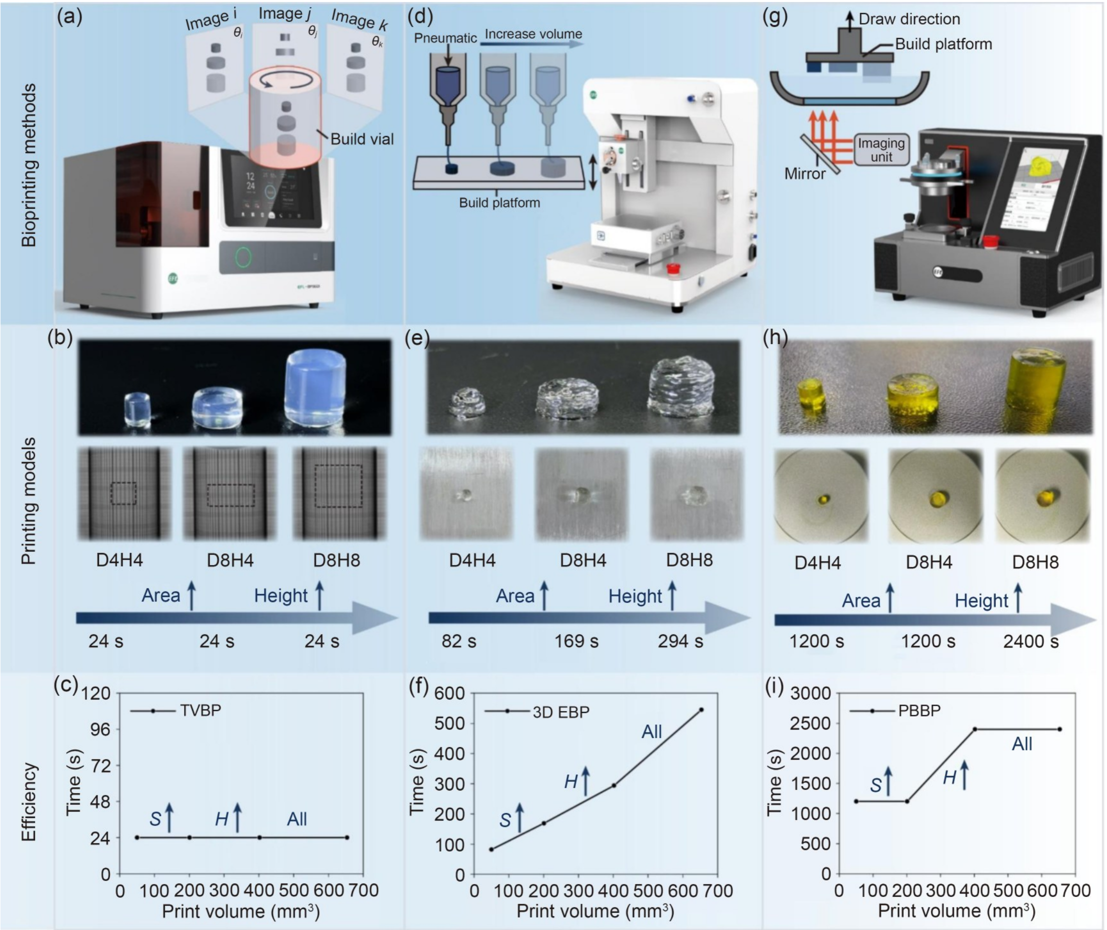

Fig. 13 Comparison of printing efficiency between 3D EBP, PBBP, and TVBP. (a) Schematic of TVBP. (b) Three cylinders printed by the EFL-BP9601 printer. (c) The printing time required in TVBP. (d) Schematic of 3D EBP. (e) Three cylinders printed by the EFL-BP6601 printer. (f) The printing time required in 3D EBP. (g) Schematic of PBBP. (h) Three cylinders printed by the EFL-BP8601 printer. (i) The printing time required in PBBP. *S*: the cross-sectional area of the printing model; *H*: the height of the printing model

rather than geometric dimensional parameters. Even when considering advanced DLP variants like continuous liquid interface printing, their theoretical maximum speed remains one order of magnitude lower than TVP. This breakthrough time efficiency stems from two core elements: (1) the achievement of high-efficiency light energy utilization through photochemical optimization enables single-exposure coverage of the entire build volume; (2) tomographic projection technology forms 3D dose distributions through angular superposition, eliminating time losses caused by mechanical motion.

Additionally noteworthy is that Orth et al. [121] achieved spatiotemporal synchronization of manufacturing and metrology through real-time scattering tomographic imaging, obtaining 3D model reconstructions with dimensional errors below 1% during the printing process. This in situ monitoring capability not only eliminates the additional time cost required by traditional ex situ metrology but, more importantly, provides the physical foundation for real-time closed-loop control. When combined with wavelength selection strategies guided by photochemical action spectra, the system can dynamically optimize light dose distribution parameters to ensure dimensional accuracy while maintaining high-speed manufacturing. This multidimensional synergistic effect enables TVBP to demonstrate unique value in interdisciplinary medical engineering fields. In biomanufacturing scenarios, it simultaneously enables ultraviolet damage reduction through red-shifted wavelengths and accomplishes centimeter-scale tissue structure construction within second-level timeframes, providing a technical pathway that integrates both efficiency and biocompatibility for complex applications such as organ printing.

5 Applications in the biomedical field

5.1 Scaffolds for tissue engineering

In the field of tissue engineering, TVBP is reshaping the paradigm for constructing complex biological structures through its unique ultrafast forming capabilities and multi-material integration. Recent advancements have progressively overcome the limitations of traditional 3D printing, enabling rapid and precise printing of cell-laden constructs.

In bone tissue engineering, Gehlen et al. [98] optimized a 5% (0.05 g/mL) GelMA+0.05% (0.0005 g/mL) LAP bioink, whose low stiffness promoted 3D cell–matrix remodeling of human mesenchymal stem cells (hMSCs). Prevascularized channels formed by co-cultured human umbilical vein endothelial cells (HUVECs) developed continuous endothelial monolayers under perfusion, significantly upregulating early osteocyte markers PDPN/DMP1. Duquesne et al. [126] developed step-growth norbornene-functionalized gelatin and thiolated gelatin, which outperformed traditional GelMA in crosslinking efficiency at identical photoinitiator concentrations. The printed structures demonstrated 3-fold volumetric stiffness and enhanced osteoinductive capacity, with substantial calcium deposition by high-viability dental pulp stem cells after 21 d. Bernal et al. [21] demonstrated a breakthrough in replicating macroscopic anatomical structures via volumetric printing. A trabecular bone model (8.5 mm×9.3 mm) reconstructed from micro-computed tomography (μCT) scans achieved a feature resolution of (144.69±13.55) μm (Fig. 14a). Its interconnected porous network supported the co-culture of endothelial colony forming cells (ECFCs) and mesenchymal stromal cells (MSCs), inducing early vascular sprout formation. A meniscus model printed at a cell density of 10^7 cells/mL exhibited a significant increase in compressive modulus ((266.54± 4.49) kPa) after 28 d of culture, matching human articular tissue properties, with uniform deposition of glycosaminoglycans (GAGs) and collagen type I/II (Fig. 14b). This rapid (<30 s) fabrication of centimeter-scale structures offers a novel pathway for clinical-scale graft production. Recently, Florczak et al. [123] devised the generative, adaptive, context-aware 3D printing (GRACE) system, which employs light-sheet microscopy to identify pre-printed structures in real time (e.g., MSC-laden femoral models) and automatically generates parametric cartilage layers for heterogeneous tissue printing. Multi-component tissues with proper matrix distribution were formed after post-culture (Fig. 14c). In addition, Chansoria et al. [127] deployed finite element modeling within an algorithmic design framework to computationally model auxetic architectures, achieving multi-material volumetric printing via thiol-ene chemistry. This enabled integration of auxetic lattices with cardiac models and fabrication of biomimetic alveolar structures. Viola et al. [108] exploited the temperature-responsive properties of two thermosensitive hydrogels (GelMA and silk fibroin methacryloyl combined with pNIPAM) to create approximately 50 μm open channels via volumetric printing. Their sizes were reduced by about 40% from room temperature to 37 °C, and compressive moduli increased by 2.8-fold and 5.1-fold at 37 °C, offering new strategies for designing complex, high-resolution tubular structures that mimic native tissue microenvironments.

The complex structure of biomimetic tissue often requires the combination of multiple process methods. Größbacher et al. [128] developed the volumetric printing across the melt electrowritten (VolMEW) technique, which successfully integrated melt electrowritten (MEW) microfiber networks with GelMA hydrogels. By modulating the electrowritten grid design, this method controlled the tensile, bursting, and bending properties of tubular structures while achieving high-resolution hydrogel encapsulation within opaque MEW scaffolds. Through sequential volumetric bioprinting, a tri-layer biomimetic vascular model was constructed—comprising an inner HUVEC endothelial cell layer, two outer GelMA layers encapsulating hMSCs, and an embedded MEW scaffold (Fig. 14d)—effectively mimicking the stratified architecture of natural blood vessels. Recently, Jones et al. [129] combined a volumetric 3D-printed (VP) polycaprolactone (PCL) metamaterial with an MEW mesh to fabricate a reinforced cardiac tissue patch (RCPatch) for intraventricular myocardial repair, addressing limitations of non-degradable clinical materials like bovine pericardial patches. The VP-fabricated anisotropic metamaterial, computationally optimized to mimic myocardial stiffness, supports cardiomyocyte infiltration and viability within a fibrin hydrogel. The MEW mesh, infused with hydrogel to reduce permeability, enables suturing and withstands intraventricular pressures. In an acute porcine model, the RCPatch sealed ventricular defects, prevented bleeding, and partially restored hemodynamics under physiological pressure, demonstrating a scalable approach for implantable, regenerative cardiac repair (Fig. 14e). Leveraging the embedded multi-material stacking advantage of volumetric printing, extrusion printing has also been combined with volumetric approaches [97] to spatially pattern multiple ink/cell types, facilitating the creation of synthetic biology-inspired cell communication models. For instance, adipocyte differentiation has been regulated by photogenetically engineered pancreatic cells [130].

Notably, TVP has achieved breakthroughs in ultra-precision optical device fabrication due to its layerless forming characteristics. By integrating tomographic projection, meniscus equilibrium effects, and iterative learning algorithms, a low-cost, rapid printing process for micro-lenses was developed. Millimeter-scale spherical lenses formed within 2 s exhibited <5 μm peak-valley contour errors, a root mean square (RMS) roughness of 0.614 nm, and an imaging resolution of 203.2 lp/mm [131]. Further combining post-curing processes (Fig. 15a), complex spherical lenses were manufactured at a rate of 3.1×10^4 mm^3/h (Fig. 15b). These lenses achieved an RMS surface roughness of

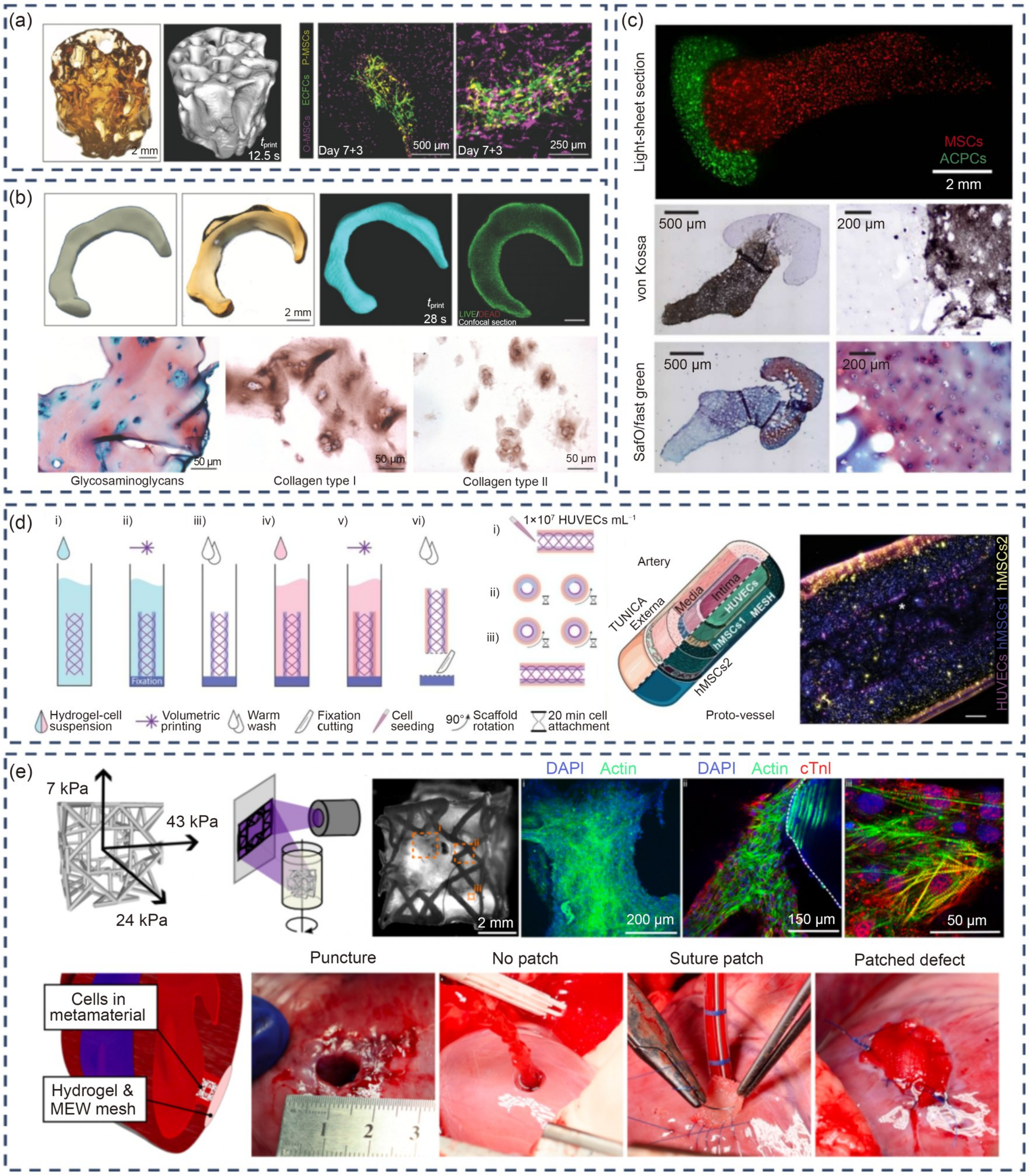

Fig. 14 Applications in tissue engineering bionics. (a) A complex trabecular bone model was fabricated, and then seeded with ECFCs (green) and P-MSCs (yellow) to induce capillary formation. (b) Long-term culture of meniscus-shaped, volumetric bioprinted constructs to assess matrix synthesis and neotissue formation. (c) A light sheet section of the construct immediately following printing with the automatically aligned femur-cartilage model showing distinct osteal and chondral regions, and the corresponding histological sections. (d) Sequential VolMEW printing of cell-laden, multi-material, and multi-layer tubular constructs. (e) Acute large animal trial using the RCPatch to repair an induced myocardial defect. P-MSCs: MSCs that act as pericytes. (a, b) are reproduced from [21], licensed under CC BY-NC-ND; (c) is reproduced from [123], licensed under CC BY 4.0; (d) is reproduced from [128], licensed under CC BY; (e) is reproduced from [129], licensed under CC BY

0.334 nm and were successfully integrated into smartphones for high-precision imaging [132]. The introduction of blurred tomography eliminated layer artifacts, enabling efficient production of freeform optical elements such as plano-convex lenses (Fig. 15c) and biconvex micro-lens arrays with performance comparable to commercial glass (Fig. 15d). Its dual-surface fabrication and fiber-overprinting capabilities open new avenues for freeform optical systems [133]. Inspired by these advancements, TVBP is poised to become a reliable method for manufacturing bio-lenses with optically tunable properties. Potential applications include bioengineered intraocular lens (IOL) (Fig. 15e) [134], corneas (Fig. 15f) [135, 136], and vitreous bodies [137], all of which demand high surface quality.

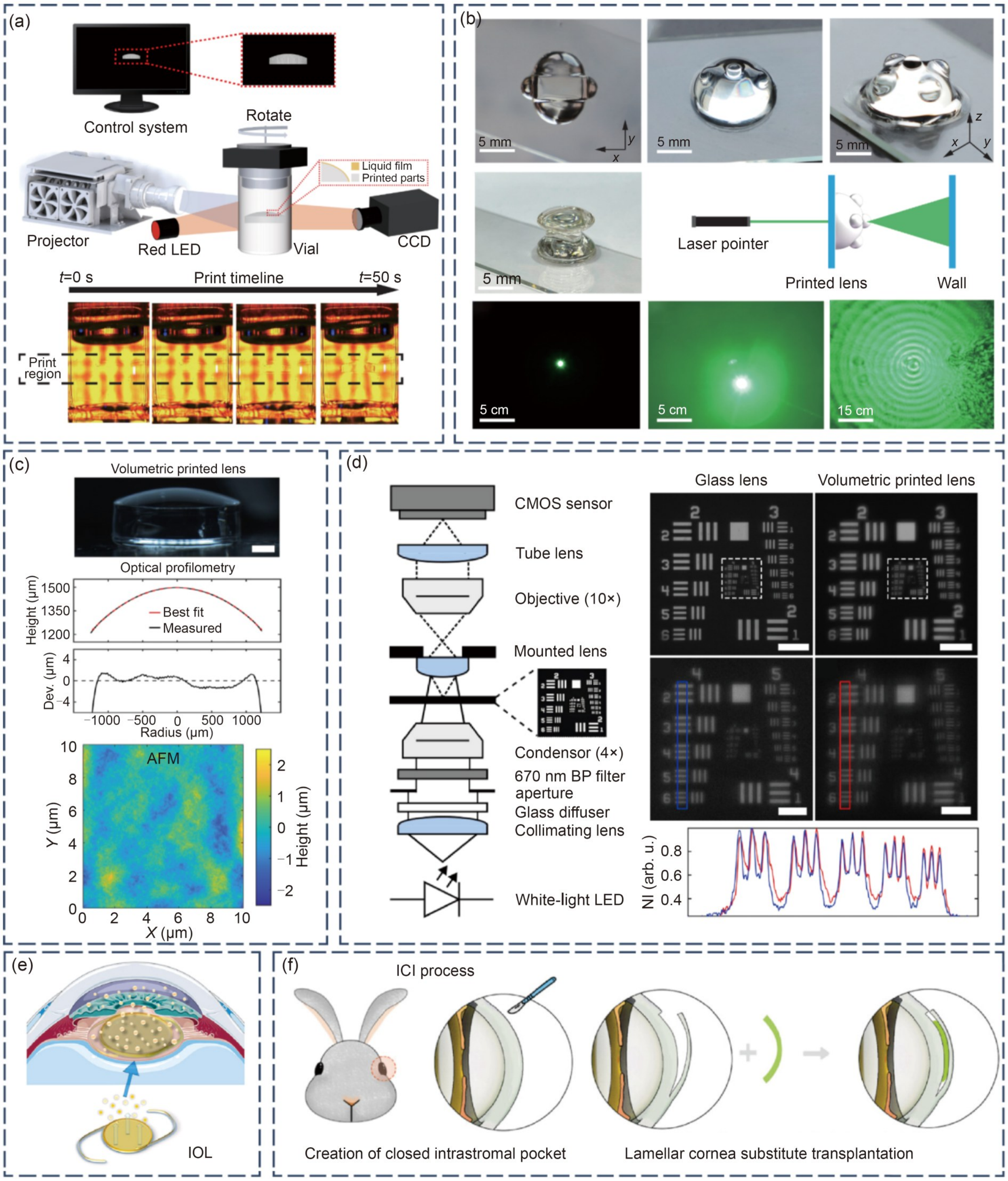

Fig. 15 Applications in precision optics and its extension in tissue engineering. (a) A centimeter-level convex lens is printed in less than a minute. (b) Fabrication of complicated lenses. (c) Optical profilometry and atomic force microscopy (AFM) measurements of the convex surface of the printed lens. (d) Image performance comparison of glass and 3D-printed lenses. (e) Schematic illustration of an IOL. (f) Process of intrastromal corneal implantation (ICI). (a, b) are reproduced from [132], licensed under CC BY 4.0; (c, d) are reproduced from [133], with permission from Optica Publishing Group under the terms of the Optica Open Access Publishing Agreement; (e) is reproduced from [134], licensed under CC BY-NC-ND; (f) is reproduced from [136], with permission from Wiley-VCH GmbH

Future integration of multi-material design, mechanical gradient modulation, and vascular network construction may accelerate the clinical translation of physiologically relevant tissue-engineered products.

5.2 Organoids and pathological models

In recent bioprinting studies, TVBP has demonstrated significant potential in constructing organoids and pathological models. Below, we analyze and elaborate on applications in organoid and disease model fabrication based on two representative studies.

Bernal et al. [101] employed TVBP combined with organoid technology to successfully fabricate complex bioarchitectures mimicking human liver functions (Figs. 16a and 16b). This study focused on printing organoid-laden gelatin hydrogels into intricate 3D structures within 20 s using TVBP. The use of optically tuned bioinks effectively addressed refractive index matching for intracellular structures, significantly mitigating printing resolution degradation caused by cell-mediated light scattering. This innovative approach preserved high organoid viability while precisely maintaining native morphology and polarity, circumventing mechanical stress-induced cellular damage common in conventional methods (Figs. 16c and 16d). Furthermore, the study proposed stiffness modulation of hydrogels to optimize hepatic organoid growth and differentiation. Results revealed that low-stiffness gelatin hydrogels (<2 kPa) actively promoted organoid differentiation, whereas stiffer materials impaired growth and suppressed liver fibrosis marker expression. This technology ultimately established a high-efficiency platform for metabolic and drug screening in liver models, with fine structural tuning enhancing liver-specific ammonia detoxification, thereby advancing applications of TVBP in organoid engineering and personalized drug testing.

Sgarminato et al. [138] applied TVBP to simulate pancreatic ductal adenocarcinoma (PDAC) microenvironments (Figs. 16e and 16f). Researchers first printed fibroblast-laden hydrogel architectures replicating pancreatic exocrine gland structures and subsequently incorporated *KRAS* oncogene-expressing human pancreatic ductal epithelial cells (HPDE-KRAS) to recapitulate tumor-stroma interactions (Fig. 16g). The co-culture of HPDE-KRAS cells with TVBP-printed fibroblast structures enabled rapid formation of dense acinar structures within days, maintaining cell viability while reproducing tumor-stromal crosstalk. This created a high-throughput, reproducible in vitro platform for analyzing early PDAC mechanisms. Immunofluorescence analysis revealed progressive myofibroblast phenotypic shifts in stromal cells, indicative of stromal activation during tumor progression. Further experiments demonstrated fibroblast-induced interleukin (IL)-6 upregulation in HPDE-KRAS co-cultures, aligning with tumor-associated myofibroblast activation signatures and serving as a biomarker for early disease progression and drug efficacy monitoring. This work highlights the utility of TVBP in constructing stromal frameworks for rapid co-culture modeling, enabling complex 3D

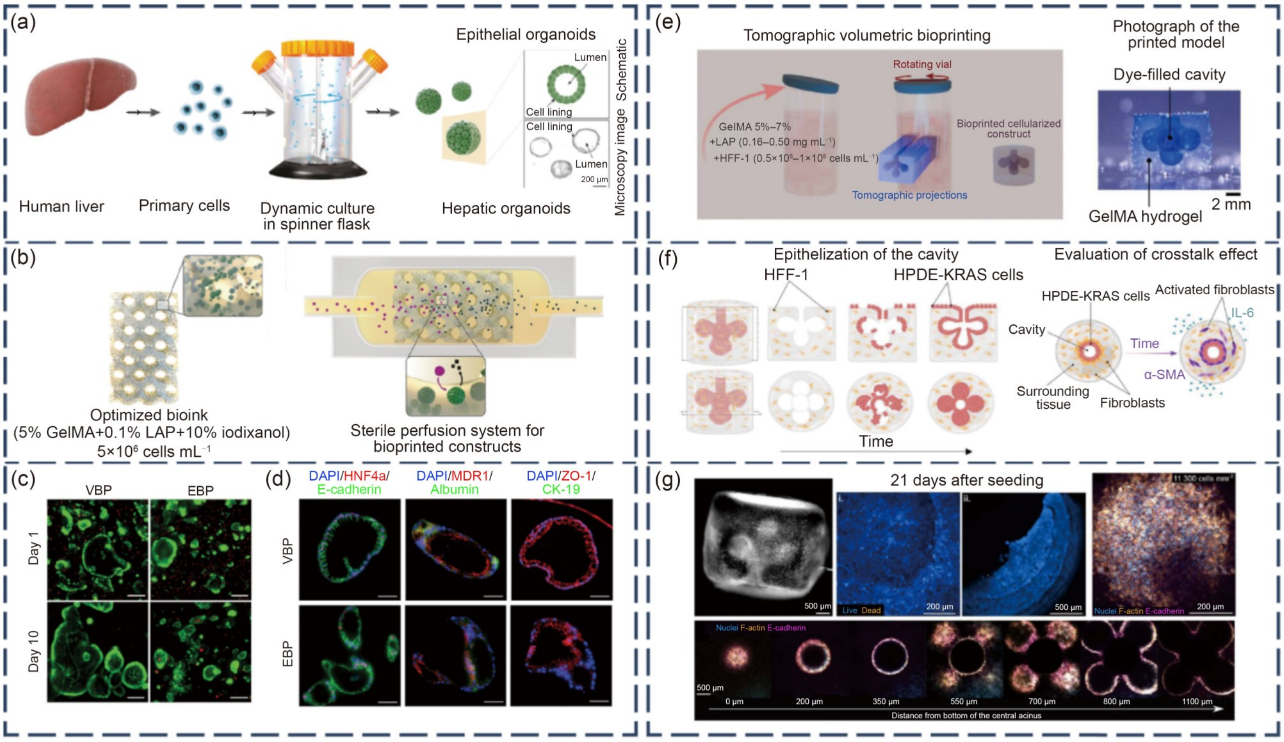

Fig. 16 Applications in organoid and pathological model construction. (a) Diagram of the hepatic organoid culture system. (b) Illustration of a complex, organoid-laden printed biofactory cultured under dynamic perfusion to enhance hepatic function. (c) Representative live/dead images; scale bars: 250 μm. (d) Representative fluorescence images of liver-specific and organoid polarization markers; scale bars: 50 μm. (e) Experimental pipeline for TVBP of pancreatic cancer models. (f) HPDE cells overexpressing the *KRAS* oncogene (HPDE-KRAS cells) are injected into fibroblast-laden bioprinted constructs, where they attach and coat the acini inner surfaces with time. (g) Epithelization of multi-acinar constructs. (a–d) are reproduced from [101], licensed under CC BY; (e–g) are reproduced from [138], licensed under CC BY 4.0

pancreatic cancer microenvironment assembly, disease progression tracking, and targeted drug evaluation.

Synthesizing these studies, TVBP exhibits distinct advantages in organoid and pathological model fabrication. First, it enables rapid fabrication of complex bio-architectures with structural precision through parameter-controlled printing, preserving cellular viability and physiological hierarchy while addressing cell damage and structural distortion inherent to traditional bioprinting. Second, high cell density and fidelity capabilities of TVBP, particularly in organoid and tumor microenvironment modeling, provide enhanced biological detail for precise investigation of cell–cell interactions and disease mechanisms. Additionally, its layerless and contactless approach minimizes cellular perturbation, better preserving the self-organizing properties of organoids [139] and tumor models to promote functional maturation.

5.3 Medicine manufacturing

As an emerging vat photopolymerization technology, TVBP demonstrates unique potential in pharmaceutical manufacturing by overcoming the limitations of conventional techniques in speed, precision, and personalized production. In a groundbreaking study, researchers pioneered the use of TVBP to simultaneously fabricate two paracetamol-loaded 3D-printed tablets (Printlets) with annular or cylindrical geometries [140]. This system precisely controlled the photopolymerization of six resin formulations, which included PEGDA 575/700 as photoreactive monomers, water/PEG300 as diluents, and LAP as a photoinitiator. Experimental data revealed that dual-tablet synchronization was achieved within an ultra-short fabrication time of 12–32 s, with all printed constructs exhibiting sustained and stable drug release profiles. This achievement not only validated the technical feasibility of TVP for multi-dose parallel production but also demonstrated that drug release kinetics could be precisely modulated by adjusting monomer molecular weights and diluent ratios, offering a novel solution for personalized dosage customization.

Further research systematically evaluated the application boundaries of TVP (Fig. 17a) vs. traditional DLP (Fig. 17b) in fabricating hydrogel-based drug-eluting devices [141]. Six hydrogel systems were constructed using [2-(acryloyloxy)ethyl] trimethylammonium chloride, LAP, PEGDA, and paracetamol. Comparative analysis of key performance parameters revealed that volumetric printing produced scalable four-dimensional (4D) drug-eluting devices within 7.5 s (Fig. 17c), matching DLP-printed samples in drug release kinetics while outperforming them in physicochemical properties such as swelling ratio and water absorption (Fig. 17d). This combination of ultrafast fabrication and superior formulation performance makes volumetric printing particularly suitable for developing dynamic drug delivery systems that require rapid environmental responsiveness. The study also highlighted the complementary nature of the two technologies: DLP retains advantages in complex microstructure fabrication, whereas volumetric printing exhibits its revolutionary potential for high-throughput rapid production. These distinct characteristics provide a scientific basis for technology selection in diverse clinical scenarios.

Recent advances in precise drug-loading control integrated volumetric printing with nondestructive testing for

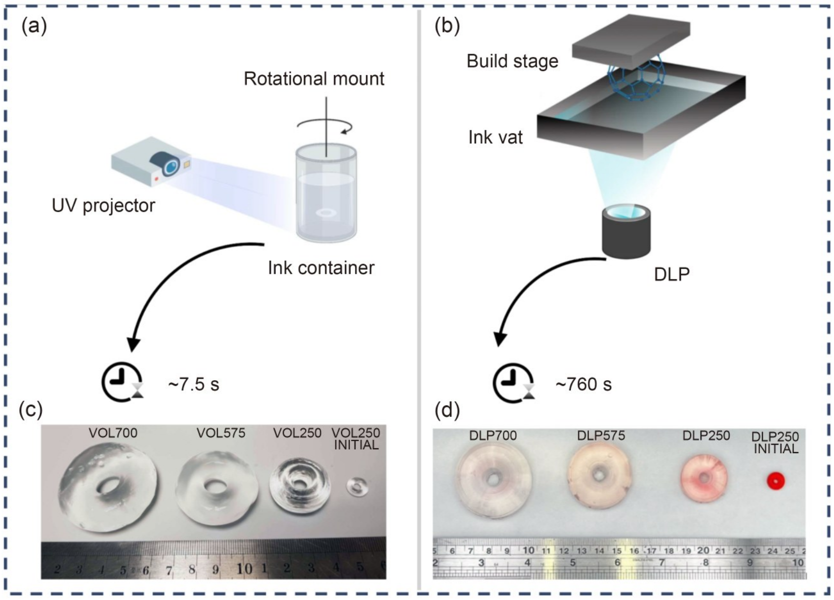

Fig. 17 Applications in medicine manufacturing. (a) TVBP takes about 7.5 s per drug delivery device. (b) DLP takes about 760 s per drug delivery device. Comparison of volumetric (c) and DLP (d) device dimensions before and after 24 h in distilled water. Reproduced from [141], licensed under CC BY 4.0

the first time to rapidly prepare water-soluble drug-loaded matrices [142]. Using warfarin as a model drug, the team optimized eight formulations with drug contents of 0.5%–6.0%, successfully fabricating annular Printlets of varying specifications in 6.5–11.1 s. The system achieved a complete dissolution-release profile of 2.5–7.0 h, coupled with precise dose control, pioneering personalized administration of water-soluble drugs.

Collectively, these studies outline the multidimensional applications of volumetric printing in pharmaceutical manufacturing: from process innovations in multi-dose parallel production to ultrafast fabrication of dynamic delivery devices and closed-loop quality control via nondestructive testing. The technology is reshaping traditional paradigms of drug production. Notably, its combination of second-scale fabrication speed and submillimeter precision enables on-demand small-batch production at the hospital pharmacy level. This technology has critical clinical value in scenarios requiring rapid dose adjustments, such as anticoagulation therapy and pediatric precision dosing. For interdisciplinary researchers, the integration of 4D shape-morphing hydrogels with volumetric printing's spatiotemporal control offers a novel platform for developing intelligent formulations, including gastrointestinal pH-responsive delivery systems and thermosensitive implants. These breakthroughs not only validate volumetric printing as a next-generation pharmaceutical technology but also establish a comprehensive "formulation design–process optimization–quality monitoring" framework, laying a robust foundation for industrializing personalized pharmacotherapy.

5.4 Flexible electronics and drives

TVBP, as an emerging layerless and high-efficiency manufacturing technology with embedded multi-material capabilities, has recently enabled multidimensional innovations in flexible electronics and actuation. In smart materials and actuation structures, thiol-ene-based shape-memory polymers have achieved layer-free fabrication of complex 3D architectures via TVBP, exemplified by self-supporting tripods and triple-arm grippers. Their near-perfect shape recovery (approximately 99%) offers novel strategies for programmable actuators [143]. For functional composite design, SonoPrint employs standing wave fields to directionally modulate the distribution of reinforcement particles (e.g., glass, metal) within photocurable resins, rapidly generating parallel lines, polygons, and other intricate patterns. This approach significantly enhances the mechanical and functional properties of materials, providing new methodologies for tissue engineering and smart composites [144].

In multi-material integration, overprinting technology combined with optical masking compensation enables precise fabrication of embedded structures. For instance, embedding endoskeleton systems within GelMA hydrogels (Fig. 18a) and leveraging swelling-induced deformation achieved 60° bending actuation of phalanges (Fig. 18b), thereby establishing a novel platform for soft robotic actuation [145]. Furthermore, TVBP facilitates multifunctional integration of flexible electronic devices through light-dose modulation and overprinting strategies. Examples include strain sensors and ionic triboelectric nanogenerators (iTENGs) based on high-viscosity ion-conductive liquids, whose exceptional transparency, conductivity, and thermal stability provide a technical foundation for liquid-free flexible electronic systems [146]. As shown in Fig. 18c, encapsulating tool center point-ionic conductive elastomer (TCP-ICE) sensors onto robotic joints enables real-time motion detection, where wires and electrodes adhere seamlessly to form a robust sensing system. Figure 18d further demonstrates the real-time acquisition of robotic hand motion signals and programmed "SOS" signal transmission, highlighting the potential of volumetric printing strategies for integrating actuation and sensing functionalities in soft robotics.

6 Outlook

Recent advancements in TVBP have centered on multimodal process integration, material innovation, and optical system development. A hybrid volumetric printing with two-photon ablation (VP-2PA) strategy combines mesoscale TVP (approximately 400 μm resolution) with two-photon ablation micromachining (approximately 2 μm resolution), enabling cross-scale integration of hierarchical vasculature in organ-on-chip systems and overcoming the inherent resolution–throughput trade-off [147]. Helical motion volumetric additive manufacturing synergizes dynamic projection offset with container rotation, achieving 650 μm feature accuracy while scaling print volumes to 3 cm×3 cm×5 cm, thereby markedly enhancing the industrial feasibility of macroscopic structures [148]. More recently, sparse-view irradiation processing volumetric additive manufacturing (SVP-VAM), employing an optimized odd–even irradiation strategy, reduced the >1000 projections required in traditional VAM to only 15, increasing the single-projection efficiency by 60 times and shortening the computing time by nearly 10 times [149].

In terms of material systems, it is essential to explore self-supporting and light-transmitting bioinks or additive components (such as gelatin or high-viscosity macromolecules) due to the influence of gravitational sedimentation during the printing process. The development of red-shifted photoinitiation systems has been particularly prominent: visible-light crosslinking systems based on Ru/SPS improved biocompatibility, whereas the introduction of boron-dipyrromethene

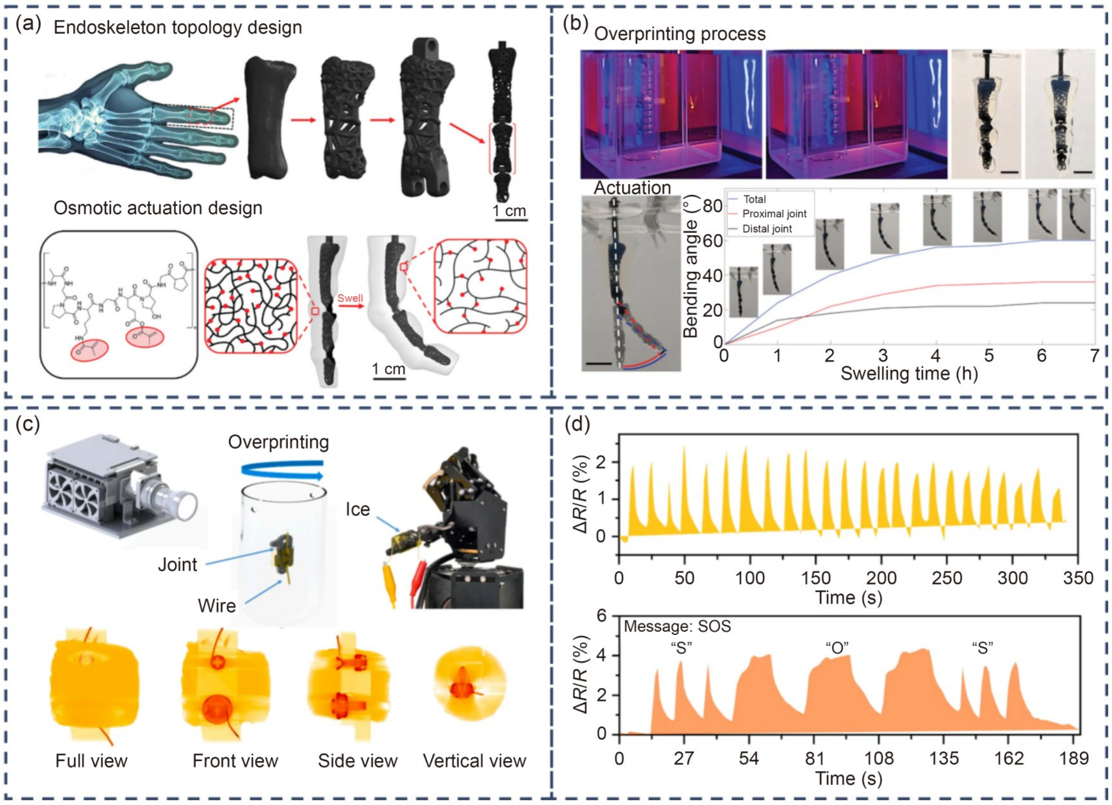

Fig. 18 Applications in flexible electronics and drives. (a) Overview and design for overprinting of the crosslinked GelMA surrounding the finger. (b) Overprinting and actuation results of the finger. (c) The sensor is overprinted on the joint. (d) Real-time acquisition of robotic hand motion signals and programmed "SOS" signal transmission. (a, b) are reproduced from [145], licensed under CC BY; (c, d) are reproduced from [146], with permission from Elsevier B.V.

(BODIPY)-based photoredox catalysts [150] and upconversion nanoparticles [151] enhanced near-infrared window light penetration capabilities. Combined with roll-to-roll (R2R) processing of thermoreversible organogel photoresists [152], these advancements provided new paradigms for continuous microstructure production. Optical system innovations include focal multiplexing projection synchronized with DMD refresh cycles to eliminate focal plane drift during dynamic patterning [152]. The liquid crystal display-based computed axial lithography (LCD-CAL) technology [153] simplifies optical architectures, reducing equipment costs by two orders of magnitude and accelerating the adoption of desktop-scale volumetric printing, bridging the gap from laboratory innovation to industrial deployment [154].

In terms of manufacturing process expansion, the integration of multi-materials is an inevitable trend. Multi-material TVP can be divided into single-step or multi-step multi-material forming. As shown in Fig. 19a, single-step multi-material printing involves distributing the inks sequentially at different positions within the printing vial during the preparation stage, while simultaneously performing projection light irradiation, achieving the integral forming of diverse structures with multiple materials [127]. It is also allowed to place embedded objects (such as MEW scaffolds [128]) inside inks in order to print multi-material scaffolds. Multi-step multi-material printing requires printing additional supports to fix positions when printing the first model. These supports can be cantilevers connected to the vial wall (Fig. 19b) [127], or a support base printed at the bottom of the model (Fig. 19c) [97]. After printing the first model, the uncured ink needs to be sucked out, and subsequent ink is added to complete the multi-material model printing. Of course, multi-step multi-material printing also allows for compounding multiple processes, such as extrusion printing [130, 155]. Extrusion printing can be performed first inside the vial, after which the position of the printed model is located via laser, and the relative position between the projection and the model is calibrated for subsequent volumetric printing, thereby achieving the forming of a multi-material model (Fig. 19d) [97]. Combining multiple fabrication techniques will amplify the embedded printing advantage of TVBP, while introducing multi-energy field-assisted curing will broaden processable material ranges and functional properties, enabling broader applications. For application innovation, organ reconstruction remains the ultimate goal in biomedical applications, while tissue regeneration scaffolds, medicine customization, and

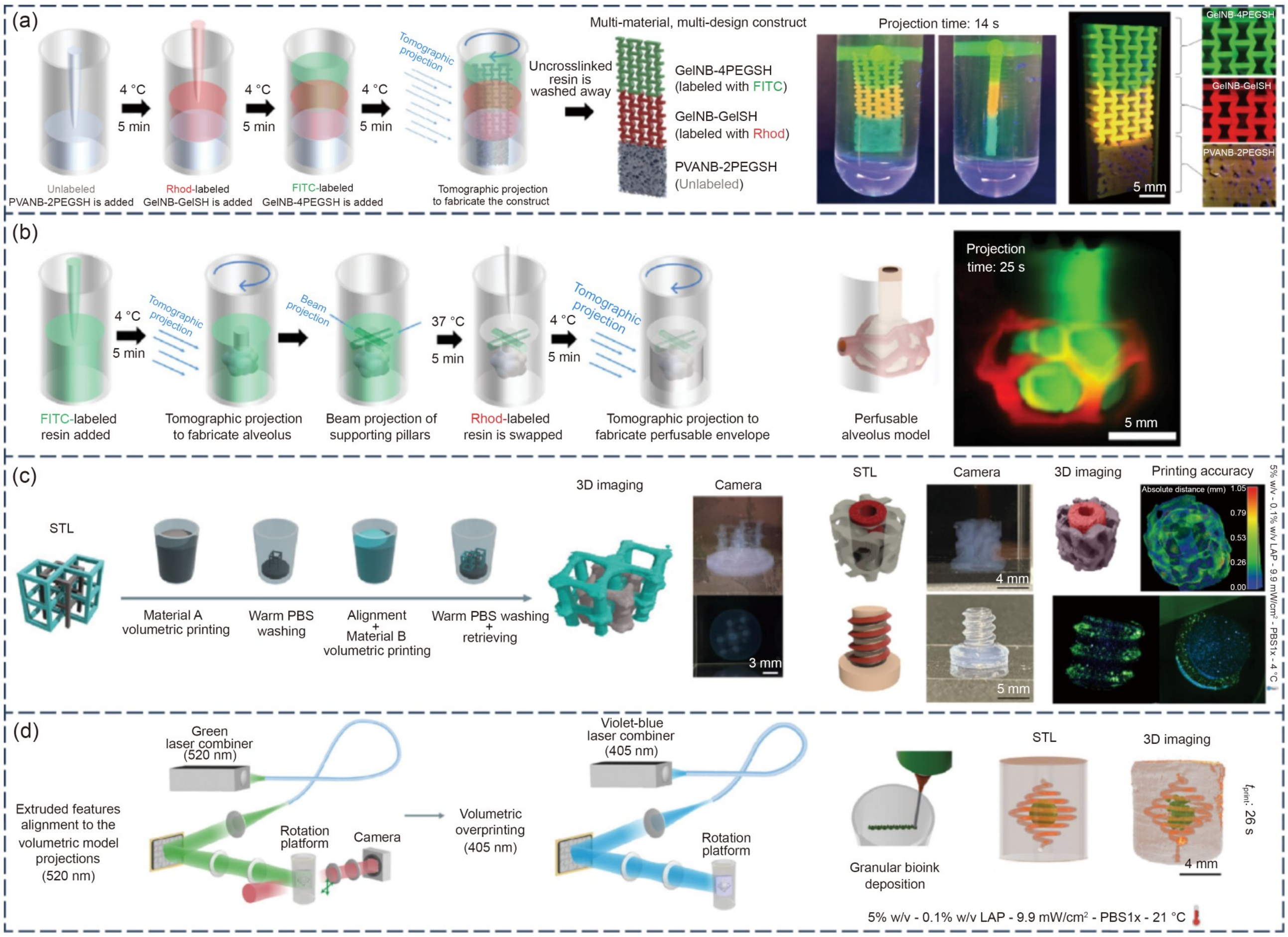

Fig. 19 Multi-material printing of TVBP. (a) Scheme of printing a three-layered construct featuring PVANB-2PEGSH, GelNB-GelSH, and GelNB-4PEGSH with different geometries across different regions and images of printing results. (b) Scheme of fabrication of the alveolar construct and images captured through light sheet microscopy (printed construct with fluorescein isothiocyanate (FITC)-labeled alveolus construct with perfused Rhod-labeled resin surrounding the construct). (c) Graphical overview of the sequential multi-material volumetric printing process, and printing examples. (d) Multi-wavelength approach for calibration and printing during EmVP and schematic representation of the EmVP process showing the fabrication of a centimeter-scale complex structure (channel diameter: 500 μm) via granular bioink extrusion. (a, b) are reproduced from [127], licensed under CC BY; (c, d) are reproduced from [97], licensed under CC BY

flexible electronics are key domains where the strengths of TVBP can be fully exploited.

Future developments in TVBP face three major challenges, as illustrated in Fig. 20:

(1) Standardization, including standardization of process parameters, material formulations, and evaluation criteria for printed outcomes;

(2) Intelligentization, incorporating artificial intelligence (AI) and achieving automation;

(3) Sustainability, encompassing material recycling, efficiency improvements, and cost control.

Looking ahead, interdisciplinary integration is reshaping the technological ecosystem of TVBP. As shown in Fig. 20, advancements in algorithmic models—such as machine learning algorithms [156]—have significantly enhanced process stability by dynamically optimizing exposure parameters and material formulations. Embedding cutting-edge technologies like machine learning and neural networks will provide real-time insights into optimizing print parameters and material selection, addressing the critical need for consistency and reliability in TVBP's workflows. Predictive analytics will deepen the understanding of how biomaterials and processing conditions influence cellular behavior [157]. This "digital twin" strategy also offers theoretical support for precision manufacturing of personalized medical devices.

Further envisioning AI-enabled TVBP, we outline four stages: design, printing, post-processing, and part evaluation (Fig. 20).

Design stage: AI assists in material formulation selection, print model optimization, and virtual system simulation [158], for example, constructing material databases and machine learning [159] models to analyze the impact of photoinitiator concentration, refractive index matching, and rheological properties on print quality.

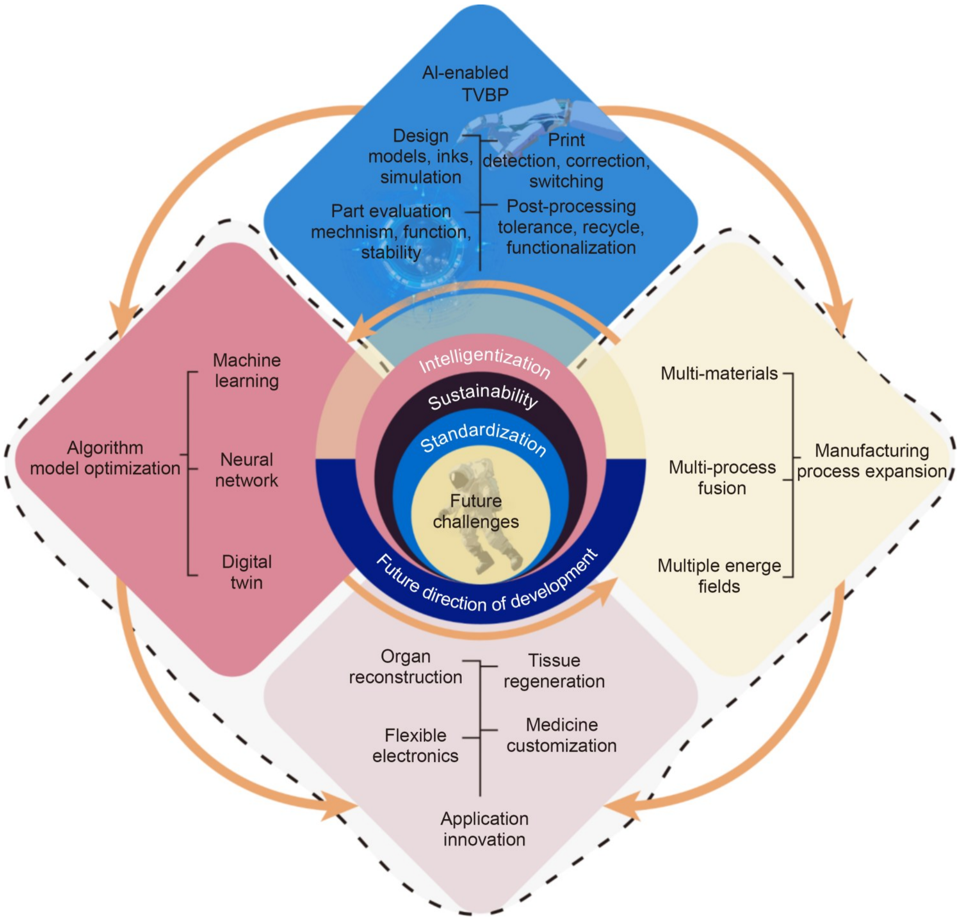

Fig. 20 Future challenges and development direction of TVBP

Printing stage: AI reduces computational complexity and uncertainty in in-situ defect detection, dynamic light-field correction, and multi-material switching [160, 161]. For instance, integrating high-speed complementary metal-oxide-semiconductor (CMOS) sensors with deep learning models enables online monitoring of projection distortions caused by resin refractive index variations. Convolutional neural networks (CNNs) [162] can reconstruct light-field distributions in real time to compensate for optical aberrations.

Post-processing stage: AI enhances reliability and repeatability in post-curing, functional modification, and uncured material recycling [163], for example, deploying recurrent neural networks to track photoinitiator degradation during ink usage, establishing a reuse cycle–crosslinking efficiency correlation model, and leveraging generative adversarial networks (GANs) [164] to synthesize virtual aging data for optimizing recycled ink blending ratios.

Part evaluation stage: AI accelerates the assessment of mechanical, functional, and stability properties. Multimodal fusion models can correlate voxel-level crosslinking density with macroscopic mechanical responses, while few-shot learning enables the prediction of compressive moduli for complex biomimetic structures with minimal experimental data, complementing time-consuming finite element method simulations [165].

7 Conclusions

TVBP is undergoing a paradigm shift from laboratory innovation to industrial application. Its unique advantages in fabrication speed, complex structure formation, and multi-material integration demonstrate its innovative potential in biomedicine, precision optics, and flexible electronics. However, technological maturation requires deep collaboration among material scientists, mechanical engineers, and clinicians. The true value of TVBP is not in replacing traditional manufacturing but rather in creating novel functional architectures that are unattainable by conventional methods. With ongoing breakthroughs in red-shifted photochemistry, AI, and precision optics, TVBP is expected to transition from rapid prototyping to functional manufacturing within the next decade, ultimately emerging as an enabling technology for multi-scale intelligent biofabrication.

Acknowledgements This work was financially supported by the National Key Research and Development Program of China (No.

2024YFB4610100), the National Natural Science Foundation of China (Nos. 52235007, T2121004, and 52325504), and the Science and Technology Planning Project of Guizhou Province (No. MS[2025] 615).

Author contributions QLW researched data for the article. All authors contributed substantially to the discussion of the content, wrote the article, and reviewed and/or edited the manuscript before submission.

Declarations

Conflict of interest YH is a deputy editor of *Bio-Design and Manufacturing* and was not involved in the editorial review or the decision to publish this article. The authors declare that they have no conflict of interest.

Ethical approval This article does not contain any studies with human or animal subjects performed by any of the authors.

Use of generative AI tools ChatGPT was used only for improving the readability and language quality of the text. All generated suggestions were reviewed, revised, and approved by authors, who assume complete responsibility for the content of the publication.

References

1. Moroni L, Burdick JA, Highley C et al (2018) Biofabrication strategies for 3D in vitro models and regenerative medicine. *Nat Rev Mater* 3(5):21–37. https://doi.org/10.1038/s41578-018-0006-y
2. Daly AC, Prendergast ME, Hughes AJ et al (2021) Bioprinting for the biologist. *Cell* 184(1):18–32. https://doi.org/10.1016/j.cell.2020.12.002
3. Murphy SV, Atala A (2014) 3D bioprinting of tissues and organs. *Nat Biotechnol* 32(8):773–785. https://doi.org/10.1038/nbt.2958
4. Chen YW, Lu WY, Zhou YY et al (2024) A spatiotemporal controllable biomimetic skin for accelerating wound repair. *Small* 20(23):2310556. https://doi.org/10.1002/smll.202310556
5. Zhang T, Sheng SH, Cai WH et al (2024) 3-D bioprinted human-derived skin organoids accelerate full-thickness skin defects repair. *Bioact Mater* 42:257–269. https://doi.org/10.1016/j.bioactmat.2024.08.036
6. Yuan X, Zhu W, Yang ZY et al (2024) Recent advances in 3D printing of smart scaffolds for bone tissue engineering and regeneration. *Adv Mater* 36(34):2403641. https://doi.org/10.1002/adma.202403641
7. Chen YW, Zou ZF, Fu T et al (2024) 3D printed grafts with gradient structures for organized vascular regeneration. *Int J Extreme Manuf* 6(3):035503. https://doi.org/10.1088/2631-7990/ad2f50
8. Li Q, Yu SY, Wang YX et al (2025). Programmable embedded bioprinting for one-step manufacturing of arterial models with customized contractile and metabolic functions. *Trends Biotechnol* 43(4):918–945. https://doi.org/10.1016/j.tibtech.2024.11.019
9. Tang H, Sun WY, Liu XC et al (2023) A bioengineered trachea-like structure improves survival in a rabbit tracheal defect model. *Sci Transl Med* 15(714):eabo4272. https://doi.org/10.1126/scitranslmed.abo4272
10. Ershad F, Rao ZL, Maharajan S et al (2025) Bioprinted optoelectronically active cardiac tissues. *Sci Adv* 11(4):eadt7210. https://doi.org/10.1126/sciadv.adt7210
11. Chen YW, Fu T, Zou ZF et al (2025) Biological reinforced concrete for cartilage repair with 3D printing. *Adv Sci* 12(16): 2416734. https://doi.org/10.1002/advs.202416734
12. Lee SJ, Jeong W, Atala A (2024) 3D bioprinting for engineered tissue constructs and patient-specific models: current progress and prospects in clinical applications. *Adv Mater* 36(49): e2408032. https://doi.org/10.1002/adma.202408032.
13. Hull CW (1986) Apparatus for production of three-dimensional objects by stereolithography. US patent US4575330A
14. Zuev DM, Nguyen AK, Putlyaev VI et al (2020) 3D printing and bioprinting using multiphoton lithography. *Bioprinting* 20: e00090. https://doi.org/10.1016/j.bprint.2020.e00090
15. He CF, Qiao TH, Wang GH et al (2024) High-resolution projection-based 3D bioprinting. *Nat Rev Bioeng* 3(2):143–158. https://doi.org/10.1038/s44222-024-00218-w
16. Yu C, Schimelman J, Wang PR et al (2020) Photopolymerizable biomaterials and light-based 3D printing strategies for biomedical applications. *Chem Rev* 120(19):10695–10743. https://doi.org/10.1021/acs.chemrev.9b00810
17. Yu K, Zhang XJ, Sun Y et al (2022) Printability during projection-based 3D bioprinting. *Bioact Mater* 11:254–267. https://doi.org/10.1016/j.bioactmat.2021.09.021
18. Shusteff M, Browar AEM, Kelly BE et al (2017) One-step volumetric additive manufacturing of complex polymer structures. *Sci Adv* 3(12):eaao5496. https://doi.org/10.1126/sciadv.aao5496
19. Kelly BE, Bhattacharya I, Heidari H et al (2019) Volumetric additive manufacturing via tomographic reconstruction. *Science* 363(6431):1075–1079. https://doi.org/10.1126/science.aau7114
20. Toombs JT, Luitz M, Cook CC et al (2022) Volumetric additive manufacturing of silica glass with microscale computed axial lithography. *Science* 376(6590):308–312. https://doi.org/10.1126/science.abm6459
21. Bernal PN, Delrot P, Loterie D et al (2019) Volumetric bioprinting of complex living-tissue constructs within seconds. *Adv Mater* 31(42):1904209. https://doi.org/10.1002/adma.201904209
22. Regehly M, Garmshausen Y, Reuter M et al (2020) Xolography for linear volumetric 3D printing. *Nature* 588(7839):620–624. https://doi.org/10.1038/s41586-020-3029-7
23. Hahn V, Rietz P, Hermann F et al (2022) Light-sheet 3D microprinting via two-colour two-step absorption. *Nat Photonics* 16(11): 784–791. https://doi.org/10.1038/s41566-022-01081-0
24. Liu H, Chansoria P, Delrot P et al (2022) Filamented light (FLight) biofabrication of highly aligned tissue-engineered constructs. *Adv Mater* 34(45):2204301. https://doi.org/10.1002/adma.202204301
25. Jones LS, Filippi M, Michelis MY et al (2024) Multidirectional filamented light biofabrication creates aligned and contractile cardiac tissues. *Adv Sci* 11(47):2404509. https://doi.org/10.1002/advs.202404509
26. Habibi M, Foroughi S, Karamzadeh V et al (2022) Direct sound printing. *Nat Commun* 13(1):1800. https://doi.org10.1038/s41467-022-29395-1
27. Kuang X, Rong QZ, Belal S et al (2023) Self-enhancing sono-inks enable deep-penetration acoustic volumetric printing. *Science* 382(6675):1148–1155. https://doi.org/10.1126/science.adi1563
28. Derayatifar M, Habibi M, Bhat R et al (2024) Holographic

direct sound printing. *Nat Commun* 15(1):6691. https://doi.org/10.1038/s41467-024-50923-8

29. Bernal PN, Florczak S, Inacker S et al (2025) The road ahead in materials and technologies for volumetric 3D printing. *Nat Rev Mater* 10:826–841. https://doi.org/10.1038/s41578-025-00785-3
30. Tumbleston JR, Shirvanyants D, Ermoshkin N et al (2015) Continuous liquid interface production of 3D objects. *Science* 347(6228):1349–1352. https://doi.org/10.1126/science.aaa2397
31. Wu JJ, Guo J, Linghu CH et al (2021) Rapid digital light 3D printing enabled by a soft and deformable hydrogel separation interface. *Nat Commun* 12(1):6070. https://doi.org/10.1038/s41467-021-26386-6
32. Loterie D, Delrot P, Moser C (2020) High-resolution tomographic volumetric additive manufacturing. *Nat Commun* 11(1): 852. https://doi.org/10.1038/s41467-020-14630-4
33. Madrid-Wolff J, Toombs J, Rizzo R et al (2023) A review of materials used in tomographic volumetric additive manufacturing. *MRS Commun* 13(5):764–785. https://doi.org/10.1557/s43579-023-00447-x
34. Murphy CA, Lim KS, Woodfield TBF (2022) Next evolution in organ-scale biofabrication: bioresin design for rapid high-resolution vat polymerization. *Adv Mater* 34(20):2107759. https://doi.org/10.1002/adma.202107759
35. Krumins E, Lentz JC, Sutcliffe B et al (2024) Glycerol-based sustainably sourced resin for volumetric printing. *Green Chem* 26(3):1345–1355. https://doi.org/10.1039/D3GC03607C
36. Cook CC, Fong EJ, Schwartz JJ et al (2020) Highly tunable thiol-ene photoresins for volumetric additive manufacturing. *Adv Mater* 32(47):2003376. https://doi.org/10.1002/adma.202003376
37. Thijssen Q, Quaak A, Toombs J et al (2023) Volumetric printing of thiol-ene photo-cross-linkable poly(ε-caprolactone): a tunable material platform serving biomedical applications. *Adv Mater* 35(19):2210136. https://doi.org/10.1002/adma.202210136
38. Falandt M, Bernal PN, Dudaryeva O et al (2023) Spatial-selective volumetric 4D printing and single-photon grafting of biomolecules within centimeter-scale hydrogels via tomographic manufacturing. *Adv Mater Technol* 8(15):202300026. https://doi.org/10.1002/admt.202300026
39. Barbera L, Madrid-Wolff J, Emma R et al (2024) Multimaterial volumetric printing of silica-based glasses. *Adv Mater Technol* 9(7):2202117. https://doi.org/10.1002/admt.202202117
40. Aizarna-Lopetegui U, Größbacher G, Herrero-Ruiz A et al (2025) Hybrid plasmonic bioresins and dECM-based materials for volumetric bioprinting of vascular-inspired architectures. *ACS Appl Mater Interfaces* 17(25):36982–36991. https://doi.org/10.1021/acsami.5c03880
41. Madrid-Wolff J, Boniface A, Loterie D et al (2022) Controlling light in scattering materials for volumetric additive manufacturing. *Adv Sci* 9(22):2105144. https://doi.org/10.1002/advs.202105144
42. Kollep M, Konstantinou G, Madrid-Wolff J et al (2022) Tomographic volumetric additive manufacturing of silicon oxycarbide ceramics. *Adv Eng Mater* 24(7):2101345. https://doi.org/10.1002/adem.202101345
43. Wang B, Engay E, Stubbe PR et al (2022) Stiffness control in dual color tomographic volumetric 3D printing. *Nat Commun* 13(1):367. https://doi.org/10.1038/s41467-022-28013-4
44. Xie MB, Lian LM, Mu X et al (2023) Volumetric additive manufacturing of pristine silk-based (bio)inks. *Nat Commun* 14(1): 210. https://doi.org/10.1038/s41467-023-35807-7
45. Qiu WW, Gehlen J, Bernero M et al (2023) A synthetic dynamic polyvinyl alcohol photoresin for fast volumetric bioprinting of functional ultrasoft hydrogel constructs. *Adv Funct Mater* 33(20):2214393. https://doi.org/10.1002/adfm.202214393
46. Dranseike D, Cui YF, Ling AS et al (2025) Dual carbon sequestration with photosynthetic living materials. *Nat Commun* 16(1): 3832. https://doi.org/10.1038/s41467-025-58761-y
47. Chansoria P, Rizzo R, Rütsche D et al (2024) Light from afield: fast, high-resolution, and layer-free deep vat 3D printing. *Chem Rev* 124(14):8787–8822. https://doi.org/10.1021/acs.chemrev.4c00134
48. Whyte DJ, Doeven EH, Sutti A et al (2024) Volumetric additive manufacturing: a new frontier in layer-less 3D printing. *Addit Manuf* 84:104094. https://doi.org/10.1016/j.addma.2024.104094
49. Kim D, Kang D, Kim D et al (2023) Volumetric bioprinting strategies for creating large-scale tissues and organs. *MRS Bull* 48(6):657–667. https://doi.org/10.1557/s43577-023-00541-4
50. Jing SB, Lian LM, Hou YY et al (2024) Advances in volumetric bioprinting. *Biofabrication* 16(1):012004. https://doi.org/10.1088/1758-5090/ad0978
51. Murshed H (2024) Intensity modulated and image guided radiation therapy. In: Fundamentals of Radiation Oncology (4th Ed.). Elsevier, p.83–94. https://doi.org/10.1016/b978-0-443-22208-5.00006-8
52. Cho B (2018) Intensity-modulated radiation therapy: a review with a physics perspective. *Radiat Oncol J* 36(1):1–10. https://doi.org/10.3857/roj.2018.00122
53. Zhang YJ, de Haan H, Houlahan K et al (2025) Impact of oxygen inhibition on (meth)acrylate photopolymerization in tomographic volumetric printing. *Addit Manuf* 109:104844. https://doi.org/10.1016/j.addma.2025.104844
54. Bhattacharya I, Toombs J, Taylor H (2021) High fidelity volumetric additive manufacturing. *Addit Manuf* 47:102299. https://doi.org/10.1016/j.addma.2021.102299
55. Rackson CM, Champley KM, Toombs JT et al (2021) Object-space optimization of tomographic reconstructions for additive manufacturing. *Addit Manuf* 48:102367. https://doi.org/10.1016/j.addma.2021.102367
56. Zhang YC, Liu MZ, Liu H et al (2023) Edge-enhanced object-space model optimization of tomographic reconstructions for additive manufacturing. *Micromachines* 14(7):1362. https://doi.org/10.3390/mi14071362
57. Webber D, Zhang YJ, Picard M et al (2023) Versatile volumetric additive manufacturing with 3D ray tracing. *Opt Express* 31(4):5531–5546. https://doi.org/10.1364/OE.481318
58. Orth A, Webber D, Zhang YJ et al (2023) Deconvolution volumetric additive manufacturing. *Nat Commun* 14(1):4412. https://doi.org/10.1038/s41467-023-39886-4
59. Chen TH, You ST, Xu L et al (2024) High-fidelity tomographic additive manufacturing for large-volume and high-attenuation situations using expectation maximization algorithm. *Addit Manuf* 80:103968. https://doi.org/10.1016/j.addma.2024.103968
60. Wechsler F, Gigli C, Madrid-Wolff J et al (2024) Wave optical model for tomographic volumetric additive manufacturing. *Opt Express* 32(8):14705–14712.

https://doi.org/10.1364/OE.521322
61. Herman GT (2009) Fundamentals of Computerized Tomography: Image Reconstruction from Projections (2nd Ed.). Springer, London, UK. https://doi.org/10.1007/978-1-84628-723-7
62. Li CC, Toombs J, Taylor HK et al (2024) Tomographic projection optimization for volumetric additive manufacturing with general band constraint Lp-norm minimization. *Addit Manuf* 94: 104447. https://doi.org/10.1016/j.addma.2024.104447
63. Nicolet B, Wechsler F, Madrid-Wolff J et al (2024) Inverse rendering for tomographic volumetric additive manufacturing. *ACM Trans Graph* 43(6):228. https://doi.org/10.1145/3687924
64. Álvarez-Castaño MI, Madsen AG, Madrid-Wolff J et al (2025) Holographic tomographic volumetric additive manufacturing. *Nat Commun* 16(1):1551. https://doi.org/10.1038/s41467-025-56852-4
65. Glückstad J, Gejl Madsen AE (2024) HoloTile light engine: new digital holographic modalities and applications. *Rep Prog Phys* 87(3):034401. https://doi.org/10.1088/1361-6633/ad2aca
66. Groll J, Burdick JA, Cho DW et al (2019) A definition of bioinks and their distinction from biomaterial inks. *Biofabrication* 11(1):013001. https://doi.org/10.1088/1758-5090/aaec52
67. Loebel C, Rodell CB, Chen MH et al (2017) Shear-thinning and self-healing hydrogels as injectable therapeutics and for 3D-printing. *Nat Protoc* 12(8):1521–1541. https://doi.org/10.1038/nprot.2017.053
68. Gillispie G, Prim P, Copus J et al (2020) Assessment methodologies for extrusion-based bioink printability. *Biofabrication* 12(2):022003. https://doi.org/10.1088/1758-5090/ab6f0d
69. Zhang YS, Haghiashtiani G, Hübscher T et al (2021) 3D extrusion bioprinting. *Nat Rev Meth Primers* 1:75. https://doi.org/10.1038/s43586-021-00073-8
70. Moroni L, Boland T, Burdick JA et al (2018) Biofabrication: a guide to technology and terminology. *Trends Biotechnol* 36(4): 384–402. https://doi.org/10.1016/j.tibtech.2017.10.015
71. He CF, Sun Y, Liu N et al (2023) Formation theory and printability of photocurable hydrogel for 3D bioprinting. *Adv Funct Mater* 33(29):2301209. https://doi.org/10.1002/adfm.202301209
72. Kirkpatrick BE, Hach GK, Nelson BR et al (2024) Photochemical control of network topology in PEG hydrogels. *Adv Mater* 36(46):2409603. https://doi.org/10.1002/adma.202409603
73. Lee M, Rizzo R, Surman F et al (2020) Guiding lights: tissue bioprinting using photoactivated materials. *Chem Rev* 120(19): 10950–11027. https://doi.org/10.1021/acs.chemrev.0c00077
74. Rizzo R, Petelinšek N, Bonato A et al (2023) From free-radical to radical-free: a paradigm shift in light-mediated biofabrication. *Adv Sci* 10(8):2205302. https://doi.org/10.1002/advs.202205302
75. Tibbitt MW, Kloxin AM, Sawicki L et al (2013) Mechanical properties and degradation of chain and step polymerized photodegradable hydrogels. *Macromolecules* 46(7):2785–2792. https://doi.org/10.1021/ma302522x
76. Qin XH, Ovsianikov A, Stampfl J et al (2014) Additive manufacturing of photosensitive hydrogels for tissue engineering applications. *BioNanoMaterials* 15(3–4):49–70. https://doi.org/10.1515/bnm-2014-0008
77. Torgersen J, Qin XH, Li ZQ et al (2013) Hydrogels for two-photon polymerization: a toolbox for mimicking the extracellular matrix. *Adv Funct Mater* 23(36):4542–4554. https://doi.org/10.1002/adfm.201203880
78. Müller MZ, Bernero M, Xie C et al (2025) Cell-guiding microporous hydrogels by photopolymerization-induced phase separation. *Nat Commun* 16(1):4923. https://doi.org/10.1038/s41467-025-60113-9
79. Northrop BH, Coffey RN (2012) Thiol-ene click chemistry: computational and kinetic analysis of the influence of alkene functionality. *J Am Chem Soc* 134(33):13804–13817. https://doi.org/10.1021/ja305441d
80. Cuthbert J, Wanasinghe SV, Matyjaszewski K et al (2021) Are RAFT and ATRP universally interchangeable polymerization methods in network formation? *Macromolecules* 54(18): 8331–8340. https://doi.org/10.1021/acs.macromol.1c01587
81. Thijssen Q, Ortega AJ, Vieira RP et al (2024) Radical inhibition in tomographic volumetric 3D printing for thiol-ene photoresists: from photorheology to printability. *React Funct Polym* 205:106096. https://doi.org/10.1016/j.reactfunctpolym.2024.106096
82. Lian LM, Xie MB, Luo ZY et al (2024) Rapid volumetric bioprinting of decellularized extracellular matrix bioinks. *Adv Mater* 36(34):e2304846. https://doi.org/10.1002/adma.202304846
83. Pien N, Bogaert B, Meeremans M et al (2025) Exploring the impact of volumetric additive manufacturing of photo-crosslinkable gelatin on mesenchymal stromal cell behavior and differentiation. *Addit Manuf* 109:104850. https://doi.org/10.1016/j.addma.2025.104850
84. Qin XH, Wang XP, Rottmar M et al (2018) Near-infrared light-sensitive polyvinyl alcohol hydrogel photoresist for spatiotemporal control of cell-instructive 3D microenvironments. *Adv Mater* 30(10):1705564. https://doi.org/10.1002/adma.201705564
85. Schwab A, Levato R, D'Este M et al (2020) Printability and shape fidelity of bioinks in 3D bioprinting. *Chem Rev* 120(19): 11028–11055. https://doi.org/10.1021/acs.chemrev.0c00084
86. Salajeghe R, Meile DH, Kruse CS et al (2023) Numerical modeling of part sedimentation during volumetric additive manufacturing. *Addit Manuf* 66:103459. https://doi.org/10.1016/j.addma.2023.103459
87. Salajeghe R, Šeta B, Marla D et al (2025) Using viscoplastic fluid to suppress part sedimentation in volumetric additive manufacturing. *Prog Addit Manuf* 10(4):2411–2422. https://doi.org/10.1007/s40964-024-00758-y
88. Riffe MB, Davidson MD, Seymour G et al (2024) Multi-material volumetric additive manufacturing of hydrogels using gelatin as a sacrificial network and 3D suspension bath. *Adv Mater* 36(34):2309026. https://doi.org/10.1002/adma.202309026
89. Hall PC, Chasko D, Wheeler T et al (2025) A versatile and high-resolution hydrogel platform for volumetric additive manufacturing based on poly(ethylene glycol) diacrylate and alginate blends. *Adv Mater Technol* 10(8):2401668. https://doi.org/10.1002/admt.202401668
90. Toombs JT, Shan IK, Taylor HK (2023) Ethyl cellulose-based thermoreversible organogel photoresist for sedimentation-free volumetric additive manufacturing. *Macromol Rapid Commun* 44(7):2200872. https://doi.org/10.1002/marc.202200872
91. Webber D, Orth A, Vidyapin V et al (2024) Printing of low-viscosity materials using tomographic additive manufacturing.

Addit Manuf 94:104480.
https://doi.org/10.1016/j.addma.2024.104480

92. Waddell T, Toombs J, Reilly A et al (2023) Use of volumetric additive manufacturing as an in-space manufacturing technology. *Acta Astronaut* 211:474–482.
https://doi.org/10.1016/j.actaastro.2023.06.048
93. König NF, Reuter M, Reuß M et al (2025) Xolography for 3D printing in microgravity. *Adv Mater* 37(5):2413391.
https://doi.org/10.1002/adma.202413391
94. He J, Sun Y, Gao Q et al (2023) Gelatin methacryloyl hydrogel, from standardization, performance, to biomedical application. *Adv Healthc Mater* 12(23):2300395.
https://doi.org/10.1002/adhm.202300395
95. Schuurmans CCL, Mihajlovic M, Hiemstra C et al (2021) Hyaluronic acid and chondroitin sulfate (meth)acrylate-based hydrogels for tissue engineering: synthesis, characteristics and pre-clinical evaluation. *Biomaterials* 268:120602.
https://doi.org/10.1016/j.biomaterials.2020.120602
96. Faralli A, Melander F, Larsen EKU et al (2016) Multiplexed dosing assays by digitally definable hydrogel volumes. *Adv Healthc Mater* 5(2):244–254.
https://doi.org/10.1002/adhm.201500542
97. Ribezzi D, Zegwaart JP, Van Gansbeke T et al (2025) Multi-material volumetric bioprinting and plug-and-play suspension bath biofabrication via bioresin molecular weight tuning and via multiwavelength alignment optics. *Adv Mater* 37(13):2409355.
https://doi.org/10.1002/adma.202409355
98. Gehlen J, Qiu WW, Schädli GN et al (2023) Tomographic volumetric bioprinting of heterocellular bone-like tissues in seconds. *Acta Biomater* 156:49–60.
https://doi.org/10.1016/j.actbio.2022.06.020
99. Whittaker JL, Choudhury NR, Dutta NK et al (2014) Facile and rapid ruthenium mediated photo-crosslinking of *Bombyx mori* silk fibroin. *J Mater Chem B* 2(37):6259–6270.
https://doi.org/10.1039/C4TB00698D
100. Soliman BG, Longoni A, Wang M et al (2023) Programming delayed dissolution into sacrificial bioinks for dynamic temporal control of architecture within 3D-bioprinted constructs. *Adv Funct Mater* 33(8):2210521.
https://doi.org/10.1002/adfm.202210521
101. Bernal PN, Bouwmeester M, Madrid-Wolff J et al (2022) Volumetric bioprinting of organoids and optically tuned hydrogels to build liver-like metabolic biofactories. *Adv Mater* 34(15): 2110054.
https://doi.org/10.1002/adma.202110054
102. Pouran B, Arbabi V, Bleys RL et al (2017) Solute transport at the interface of cartilage and subchondral bone plate: effect of micro-architecture. *J Biomech* 52:148–154.
https://doi.org/10.1016/j.jbiomech.2016.12.025
103. Liu PY, Chin LK, Ser W et al (2016) Cell refractive index for cell biology and disease diagnosis: past, present and future. *Lab Chip* 16(4):634–644.
https://doi.org/10.1039/C5LC01445J
104. Rizzo R, Ruetsche D, Liu H et al (2021) Optimized photoclick (bio)resins for fast volumetric bioprinting. *Adv Mater* 33(49): 2102900.
https://doi.org/10.1002/adma.202102900
105. Cianciosi A, Stecher S, Löffler M et al (2023) Flexible allyl-modified gelatin photoclick resin tailored for volumetric bioprinting of matrices for soft tissue engineering. *Adv Healthc Mater* 12(30):2300977.
https://doi.org/10.1002/adhm.202300977
106. Hasenauer A, Bevc K, McCabe MC et al (2025) Volumetric printed biomimetic scaffolds support in vitro lactation of human milk-derived mammary epithelial cells. *Sci Adv* 11(23):eadu5793.
https://doi.org/10.1126/sciadv.adu5793
107. Li CC, Toombs J, Taylor H (2020) Tomographic color Schlieren refractive index mapping for computed axial lithography. In: Proceedings of the 5th Annual Symposium on Computational Fabrication, Article 12.
https://doi.org/10.1145/3424630.3425421
108. Viola M, Valverde MG, Bernal PN et al (2024) Thermal shrinking of biopolymeric hydrogels for high resolution 3D printing of kidney tubules. *Adv Funct Mater* 34(46):2406098.
https://doi.org/10.1002/adfm.202406098
109. Levato R, Dudaryeva O, Garciamendez-Mijares CE et al (2023) Light-based vat-polymerization bioprinting. *Nat Rev Methods Primers* 3:47.
https://doi.org/10.1038/s43586-023-00231-0
110. Buchholz MB, Bernal PN, Bessler N et al (2025) Development of a bioreactor and volumetric bioprinting protocol to enable perfused culture of biofabricated human epithelial mammary ducts and endothelial constructs. *Biofabrication* 17(3):031001.
https://doi.org/10.1088/1758-5090/add20f
111. Sampsell JB (1994) Digital micromirror device and its application to projection displays. *J Vac Sci Technol B Microelectron Nanometer Struct Process Meas Phenom* 12(6):3242–3246.
https://doi.org/10.1116/1.587506
112. Ren YX, Lu RD, Gong L (2015) Tailoring light with a digital micromirror device. *Ann Der Phys* 527(7–8):447–470.
https://doi.org/10.1002/andp.201500111
113. Zhang YQ, Gross H (2019) Systematic design of microscope objectives. Part I: System review and analysis. *Adv Opt Technol* 8(5):313–347.
https://doi.org/10.1515/aot-2019-0002
114. Zhang YQ, Gross H (2019) Systematic design of microscope objectives. Part II: Lens modules and design principles. *Adv Opt Technol* 8(5):349–384.
https://doi.org/10.1515/aot-2019-0013
115. Moran BD, Fong EJ, Cook CC et al (2021) Volumetric additive manufacturing system optics. In: SPIE 11698, Emerging Digital Micromirror Device Based Systems and Applications XIII, 1169805.
https://doi.org/10.1117/12.2577670
116. Orth A, Sampson KL, Ting K et al (2021) Correcting ray distortion in tomographic additive manufacturing. *Opt Express* 29(7): 11037–11054.
https://doi.org/10.1364/OE.419795
117. Arjmand P, Katz O, Gigan S et al (2021) Three-dimensional broadband light beam manipulation in forward scattering samples. *Opt Express* 29(5):6563–6581.
https://doi.org/10.1364/OE.412640
118. Ligon SC, Husár B, Wutzel H et al (2014) Strategies to reduce oxygen inhibition in photoinduced polymerization. *Chem Rev* 114(1):557–589.
https://doi.org/10.1021/cr3005197
119. Weisgraber TH, de Beer MP, Huang SJ et al (2023) Virtual volumetric additive manufacturing (VirtualVAM). *Adv Mater Technol* 8(23):2301054.
https://doi.org/10.1002/admt.202301054
120. Orth A, Zhang YJ, Houlahan K et al (2025) Automatic exposure volumetric additive manufacturing. *Adv Mater Technol* 10(17): e02168.
https://doi.org/10.1002/admt.202402168
121. Orth A, Sampson KL, Zhang YJ et al (2022) On-the-fly 3D metrology of volumetric additive manufacturing. *Addit Manuf* 56: 102869.
https://doi.org/10.1016/j.addma.2022.102869
122. Bagheri A, Zakerzadeh MR, Sadigh MJ (2024) Occlusion-based model weighting for volumetric additive manufacturing around

inserts. *Virtual Phys Prototyp* 19(1):e2407473. https://doi.org/10.1080/17452759.2024.2407473

123. Florczak S, Größbacher G, Ribezzi D et al (2025) Adaptive and context-aware volumetric printing. *Nature* 645(8079):108–114. https://doi.org/10.1038/s41586-025-09436-7
124. Thijssen Q, Carroll JA, Feist F et al (2024) Beyond absorption maxima: the impact of wavelength-resolved photochemistry on materials science. *Mater Horiz* 11(24):6184–6191. https://doi.org/10.1039/D4MH00976B
125. Álvarez-Castaño MI, Pu Y, Moser C (2025) High light-efficiency holographic tomographic volumetric additive manufacturing using a MEMS-based phase-only light modulator. https://doi.org/10.48550/arXiv.2506.02578
126. Duquesne J, Parmentier L, Vermeersch E et al (2025) Volumetric bioprinting of the osteoid niche. *Biofabrication* 17(2):025002. https://doi.org/10.1088/1758-5090/adab25
127. Chansoria P, Rütsche D, Wang A et al (2023) Synergizing algorithmic design, photoclick chemistry and multi-material volumetric printing for accelerating complex shape engineering. *Adv Sci* 10(26):2300912. https://doi.org/10.1002/advs.202300912
128. Größbacher G, Bartolf-Kopp M, Gergely C et al (2023) Volumetric printing across melt electrowritten scaffolds fabricates multi-material living constructs with tunable architecture and mechanics. *Adv Mater* 35(32):2300756. https://doi.org/10.1002/adma.202300756
129. Jones LS, Rodriguez Cetina Biefer H, Mekkattu M et al (2025) Volumetric 3D printing and melt-electrowriting to fabricate implantable reinforced cardiac tissue patches. *Adv Mater* 37(45): 2504765. https://doi.org/10.1002/adma.202504765
130. Ribezzi D, Gueye M, Florczak S et al (2023) Shaping synthetic multicellular and complex multimaterial tissues via embedded extrusion-volumetric printing of microgels. *Adv Mater* 35(36): 2301673. https://doi.org/10.1002/adma.202301673
131. Xu Y, Huang P, To S et al (2022) Low-cost volumetric 3D printing of high-precision miniature lenses in seconds. *Adv Opt Mater* 10(17):2200488. https://doi.org/10.1002/adom.202200488
132. Peng S, Xu JW, Li DY et al (2023) Ultra-fast 3D printing of assembly: free complex optics with sub-nanometer surface quality at mesoscale. *Int J Extreme Manuf* 5(3):035007. https://doi.org/10.1088/2631-7990/acdb0d
133. Webber D, Zhang YJ, Sampson KL et al (2024) Micro-optics fabrication using blurred tomography. *Optica* 11(5):665–672. https://doi.org/10.1364/optica.519278
134. Li MN, Xu JW, Li JY et al (2023) A novel gatifloxacin-loaded intraocular lens for prophylaxis of postoperative endophthalmitis. *Bioact Mater* 20:271–285. https://doi.org/10.1016/j.bioactmat.2022.05.032
135. He BB, Wang J, Xie MT et al (2022) 3D printed biomimetic epithelium/stroma bilayer hydrogel implant for corneal regeneration. *Bioact Mater* 17:234–247. https://doi.org/10.1016/j.bioactmat.2022.01.034
136. Xue Q, Hu HY, Wang WW et al (2023) Liquid-phase integrated 3D printed biological lenses for lamellar corneal substitute. *Adv Healthc Mater* 12(27):2300600. https://doi.org/10.1002/adhm.202300600
137. Kong JS, Kim JJ, Riva L et al (2024) In vitro three-dimensional volumetric printing of vitreous body models using decellularized extracellular matrix bioink. *Biofabrication* 16(4):045030. https://doi.org/10.1088/1758-5090/ad6f46
138. Sgarminato V, Madrid-Wolff J, Boniface A et al (2024) 3D in vitro modeling of the exocrine pancreatic unit using tomographic volumetric bioprinting. *Biofabrication* 16(4):045034. https://doi.org/10.1088/1758-5090/ad6d8d
139. Wang CR, Huang MH, Lin YN et al (2023) ENO2-derived phosphoenolpyruvate functions as an endogenous inhibitor of HDAC1 and confers resistance to antiangiogenic therapy. *Nat Metab* 5(10): 1765–1786. https://doi.org/10.1038/s42255-023-00883-y
140. Rodríguez-Pombo L, Martínez-Castro L, Xu XY et al (2023) Simultaneous fabrication of multiple tablets within seconds using tomographic volumetric 3D printing. *Int J Pharm X* 5:100166. https://doi.org/10.1016/j.ijpx.2023.100166
141. Oh YC, Ong JJ, Alfassam H et al (2025) Fabrication of 3D printed mutable drug delivery devices: a comparative study of volumetric and digital light processing printing. *Drug Deliv Transl Res* 15(5):1595–1608. https://doi.org/10.1007/s13346-024-01697-5
142. Ong JJ, Jørgensen AK, Zhu Z et al (2025) Volumetric printing and non-destructive drug quantification of water-soluble supramolecular hydrogels. *Drug Deliv Transl Res* 15(6):2048–2063. https://doi.org/10.1007/s13346-024-01723-6
143. Schwartz JJ, Porcincula DH, Cook CC et al (2022) Volumetric additive manufacturing of shape memory polymers. *Polym Chem* 13(13):1813–1817. https://doi.org/10.1039/D1PY01723C
144. Agrawal P, Zhuang SY, Dreher S et al (2024) SonoPrint: acoustically assisted volumetric 3D printing for composites. *Adv Mater* 36(40):2408374. https://doi.org/10.1002/adma.202408374
145. Darkes-Burkey C, Shepherd RF (2024) Volumetric 3D printing of endoskeletal soft robots. *Adv Mater* 36(33):2402217. https://doi.org/10.1002/adma.202402217
146. Peng S, Chen GM, Luo X et al (2024) Volumetric 3D printing of ionic conductive elastomers for multifunctional flexible electronics. *Addit Manuf* 95:104536. https://doi.org/10.1016/j.addma.2024.104536
147. Rizzo R, Rütsche D, Liu H et al (2023) Multiscale hybrid fabrication: volumetric printing meets two-photon ablation. *Adv Mater Technol* 8(11):2201871. https://doi.org/10.1002/admt.202201871
148. Boniface A, Maître F, Madrid-Wolff J et al (2023) Volumetric helical additive manufacturing. *Light Adv Manuf* 4(2):124–132. https://doi.org/10.37188/lam.2023.012
149. Wang HY, Gao FY, Shi Y et al (2025) Sparse-view irradiation processing volumetric additive manufacturing. *Int J Extreme Manuf* 7(6):065001. https://doi.org/10.1088/2631-7990/adebbf
150. Stafford A, Ahn D, Raulerson EK et al (2020) Catalyst halogenation enables rapid and efficient polymerizations with visible to far-red light. *J Am Chem Soc* 142(34):14733–14742. https://doi.org/10.1021/jacs.0c07136
151. Sanders SN, Schloemer TH, Gangishetty MK et al (2022) Triplet fusion upconversion nanocapsules for volumetric 3D printing. *Nature* 604(7906):474–478. https://doi.org/10.1038/s41586-022-04485-8
152. Toombs JT, Li CC, Taylor HK (2024) Roll-to-roll tomographic volumetric additive manufacturing for continuous production of microstructures on long flexible substrates. In*:* Proceedings Volume PC12898, Advanced Fabrication Technologies for Micro/Nano Optics and Photonics XVII. https://doi.org/10.1117/12.3008445
153. Tisato S, Vera G, Mani A et al (2024) An easy-to-build, accessible volumetric 3D printer based on a liquid crystal display for rapid resin development. *Addit Manuf* 87:104232. https://doi.org/10.1016/j.addma.2024.104232
154. Somers P, Münchinger A, Maruo S et al (2023) The physics of

3D printing with light. *Nat Rev Phys* 6(2):99–113. https://doi.org/10.1038/s42254-023-00671-3

155. Tisato S, Vera G, Song QC et al (2025) Additive manufacturing of multi-material and hollow structures by embedded extrusion-volumetric printing. *Nat Commun* 16(1):6730. https://doi.org/10.1038/s41467-025-62057-6
156. Dananjaya SAV, Chevali VS, Dear JP et al (2024) 3D printing of biodegradable polymers and their composites – current state-of-the-art, properties, applications, and machine learning for potential future applications. *Prog Mater Sci* 146:101336. https://doi.org/10.1016/j.pmatsci.2024.101336
157. Mathur V, Dsouza V, Srinivasan V et al (2025) Volumetric additive manufacturing for cell printing: bridging industry adaptation and regulatory frontiers. *ACS Biomater Sci Eng* 11(1):156–181. https://doi.org/10.1021/acsbiomaterials.4c01837
158. Nam J, Kim M (2024) Advances in materials and technologies for digital light processing 3D printing. *Nano Converg* 11(1):45. https://doi.org/10.1186/s40580-024-00452-3
159. Goh GD, Yeong WY (2022) Applications of machine learning in 3D printing. *Mater Today Proc* 70:95–100. https://doi.org/10.1016/j.matpr.2022.08.551
160. Tamir TS, Xiong G, Fang QH et al (2023) Machine-learning-based monitoring and optimization of processing parameters in 3D printing. *Int J Comput Integr Manuf* 36(9):1362–1378. https://doi.org/10.1080/0951192X.2022.2145019
161. Bracco F, Zanderigo G, Paynabar K et al (2025) Leveraging transfer learning for efficient bioprinting. *Biofabrication* 17(3): 035022. https://doi.org/10.1088/1758-5090/ade62f
162. Kelly D, Sergis V, Ventura i Blanco L et al (2025) Autonomous control of extrusion bioprinting using convolutional neural networks. *Adv Funct Mater* 35(30):2424553. https://doi.org/10.1002/adfm.202424553
163. Ma L, Yu SJ, Xu XD et al (2023) Application of artificial intelligence in 3D printing physical organ models. *Mater Today Bio* 23:100792. https://doi.org/10.1016/j.mtbio.2023.100792
164. Killgore JP, Kolibaba TJ, Caplins BW et al (2023) A data-driven approach to complex voxel predictions in grayscale digital light processing additive manufacturing using U-nets and generative adversarial networks. *Small* 19(50):2301987. https://doi.org/10.1002/smll.202301987
165. Wang J, Das S, Rai R et al (2018) Data-driven simulation for fast prediction of pull-up process in bottom-up stereolithography. *Comput Aided Des* 99:29–42. https://doi.org/10.1016/j.cad.2018.02.002